Single-cell spatial mapping reveals dynamic bone marrow microarchitectural alterations and enhances clinical diagnostics in MDS

Ryan Nachman,[1] Aleksandra Kopacz,[1] Caitlin Unkenholz,[1,4] Jian Chai, [2] Arvin Ruiz,[3] Itzel Valencia,[4] Jeanne Jiang,[4] Fabio Socciarelli,[4] Jiwoon Park,[5] Christopher Mason,[(5-8)] Ling Zhang,[9] David Sallman,[10] Gail J. Roboz,[11] Pinkal Desai,[11] Justin Kaner,[11] Joshua Fein,[11] Monica Guzman,[11] Neal Lindeman,[12] Amy Chadburn,[2] Madhu Ouseph,[2,12] Paul Simonson,[2] Julia Geyer,[2] Giorgio Inghirami,[2,3] Shahin Rafii,[1] David Redmond,[1*] Sanjay Patel[2,4*]

[1]Division of Regenerative Medicine, Hartman Institute for Therapeutic Organ Regeneration, Ansary Stem Cell Institute, Department of Medicine, Weill Cornell Medicine, New York, NY, USA
[2]Division of Hematopathology, Department of Pathology and Laboratory Medicine, Weill Cornell Medicine/NewYork-Presbyterian Hospital, New York, NY, USA
[3]Immunopathology Laboratory, Weill Cornell Medical College/NewYork-Presbyterian Hospital, New York, NY, USA
[4]Multiparametric In Situ Imaging (MISI) Laboratory, Department of Pathology and Laboratory Medicine, Weill Cornell Medicine, New York, NY, USA
[5]Department of Physiology and Biophysics, Weill Cornell Medicine, New York, NY, USA
[6]The Feil Family Brain and Mind Research Institute, Weill Cornell Medicine, New York, NY
[7]WorldQuant Initiative for Quantitative Prediction, Weill Cornell Medicine, New York, NY
[8]The HRH Prince Alwaleed Bin Talal Bin Abdulaziz Alsaud Institute for Computational Biomedicine, Weill Cornell Medicine, New York, NY
[9]Department of Hematopathology and Laboratory Medicine, Moffitt Cancer Center, Tampa, FL, USA
[10]Department of Malignant Hematology, Moffitt Cancer Center, Tampa, FL, USA
[11]Division of Hematology and Medical Oncology, Department of Medicine, Weill Cornell Medicine/NewYork-Presbyterian Hospital, New York, USA
[12]Division of Molecular Genetic Pathology, Department of Pathology and Laboratory Medicine, Weill Cornell Medicine/NewYork-Presbyterian Hospital, New York

*Correspondence: Sanjay Patel, MD (sap9151@med.cornell.edu) & David Redmond, PhD (dar2042@med.cornell.edu)

ABSTRACT

Myelodysplastic neoplasms (MDS) are genetically diverse hematopoietic cancers characterized by ineffective blood cell production, peripheral cytopenias, and an increased risk of acute myeloid leukemia. Diagnosis traditionally requires subjective histomorphologic assessment of a bone marrow biopsy sample. The potential biological and/or clinical relevance of subtle microarchitectural changes, unrecognizable using conventional methods, remains unknown. Here, we applied a recently developed AI-driven, whole slide imaging-based single-cell spatial proteomic profiling method to 77 annotated MDS and precursor state bone marrow tissue samples, including longitudinal cases. Compared to age-matched controls, MDS tissues showed significant changes in progenitor cell frequencies, morphologies of erythroid precursors and megakaryocytes, HSPC displacement from vasculature, abnormal progenitor cell clustering, and disrupted erythroid islands. Some alterations correlated more closely with specific mutations (e.g., *SF3B1*, *TP53*) than clinical risk scores (IPSS-M). Using all extracted tissue features, we developed a composite spatially informed "MDS severity score", which aligned with clinical and genetic parameters across serial samples. This work uncovers previously unrecognized, genotype-linked microarchitectural alterations in MDS, the measurement of which may enhance existing diagnostic and disease monitoring strategies.

INTRODUCTION

Myelodysplastic neoplasms (MDS) develop as a result of clonal proliferation of hematopoietic stem cells and their progeny. They are defined by abnormal hematopoiesis, which manifests with peripheral cytopenias, their clinical sequelae, and a predisposition to acute leukemia.[1] A histopathologic evaluation is required to establish the diagnosis, and involves a subjective interrogation for cytologic features of dysplasia in hematopoietic cells, accompanied by overt architectural alterations in intact bone marrow trephine biopsy tissues, such as age-adjusted hypercellularity and abnormal megakaryocyte morphology.[2,3] The

cornerstones for these assessments include tools that have not evolved considerably over the last few decades, such as light microscopy, single-marker immunohistochemistry, and flow cytometric immunophenotyping.[4] It is particularly noteworthy that blast percentage, which is still derived through manual enumeration by trained practitioners, remains the only parameter incorporated into algorithms used for patient risk stratification.[5,6]

The rapidly evolving genomic era has greatly advanced our understanding of the cell-intrinsic genetic basis of MDS and led to improvements in the models currently used for patient risk stratification.[6] Nevertheless, optimal integration of morphologic, immunophenotypic, and genetic parameters remains highly controversial, as evidenced by recent struggles to harmonize the competing International Consensus Classification (ICC) and World Health Organization (WHO) MDS classification systems.[2,7] Importantly, these ancillary data are typically derived either from peripheral blood or aspirated bone marrow material, and therefore subject to artifacts of sampling, and also unable to capture information about the complex marrow microarchitecture. Despite these limitations, studies based on aspirated marrow have clearly indicated roles for cell-intrinsic *and* –extrinsic factors in MDS disease pathogenesis,[8] although reliable spatial architecture models of the disease that account for its clinical and genetic heterogeneity are still lacking.[9,10]

We recently developed an approach to perform in situ spatial mapping of human hematopoiesis using archival tissue samples, multiplex immunofluorescence tissue staining, whole slide imaging, and artificial intelligence (AI)-based image analysis at single cell resolution;[11] our analysis of a cohort of normal bone marrow samples revealed spatial patterns of hematopoiesis that were largely conserved with aging. Here, we have applied this approach, and expanded upon our analytical methodology, to profile a cohort of clinically and genetically annotated bone marrow tissue samples from MDS patients, including biopsies at multiple timepoints along the course of standard-of-care therapy. Our findings reveal known, and also previously unrecognized, quantifiable perturbations to the normal spatial microarchitecture of human hematopoiesis in MDS.

RESULTS

Characteristics of patient cohort

We assembled a cohort of clinically and genetically annotated archival bone marrow trephine biopsy samples collected as part of routine diagnostic hematopathology evaluations at our academic medical center **(Figure 1a, Supplementary Data Table 1)**. The cohort included 77 samples from 48 unique patients with MDS (n=36) or the precursor state clonal hematopoiesis of indeterminate potential/clonal cytopenia of unknown significance (CHIP/CCUS, n=12), and additionally, 29 samples from 14 MDS patients collected along the course of pharmacologic management with or without eventual allogeneic hematopoietic stem cell transplantation (HSCT). 22 normal bone marrow controls (NBMs), including age-matched samples, from a recently published cohort were also analyzed.[11]

The median age among CHIP/CCUS and MDS patients was 77, with a M:F of 1:1. MDS samples were broadly categorized into those with low-blasts (MDS-LB, n=20) or with high-blasts (MDS-IB, n=16). International Prognostic Scoring System-Molecular (IPSS-M) values were calculated for all diagnostic samples from MDS patients; IPSS-M scores ranged from –1.61 to 4.39 (median=0.285).

Quantitative and morphologic variations between normal and MDS bone marrows

Following multiplex immunofluorescence (MxIF) staining and whole slide imaging (WSI) or archival trephine biopsy tissues, individual cells and architectural structures were segmented and further characterized as previously described, resulting in a dataset of approximately 5 million single cells (**Extended Data Figure 1a-b**).[11]

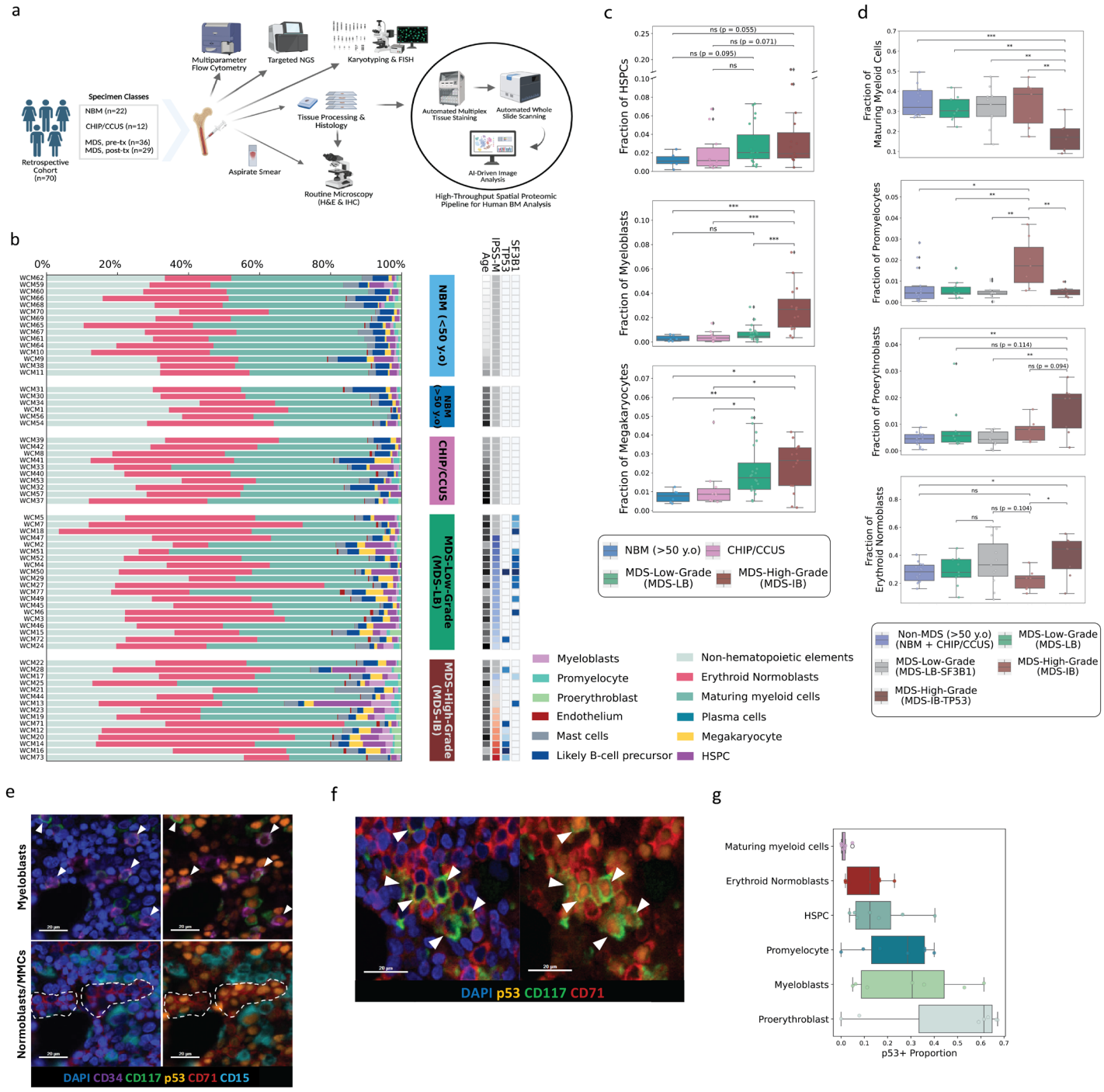
a
Multiparameter Flow Cytometry
Targeted NGS
Karyotyping & FISH
Specimen Classes
NBM (n=22)
CHIP/CCUS (n=12)
MDS, pre-tx (n=36)
MDS, post-tx (n=29)
Retrospective Cohort (n=70)
Tissue Processing & Histology
Aspirate Smear
Routine Microscopy (H&E & IHC)
Automated Multiplex Tissue Staining
Automated Whole Slide Scanning
AI-Driven Image Analysis
High-Throughput Spatial Proteomic Pipeline for Human BM Analysis
b
0%
20%
40%
60%
80%
100%
NBM (<50 y.o)
NBM (>50 y.o)
CHIP/CCUS
MDS-Low-Grade (MDS-LB)
MDS-High-Grade (MDS-IB)
Age
IPSS-M
TP53
SF3B1
Myeloblasts
Promyelocyte
Proerythroblast
Endothelium
Mast cells
Likely B-cell precursor
Non-hematopoietic elements
Erythroid Normoblasts
Maturing myeloid cells
Plasma cells
Megakaryocyte
HSPC
c
Fraction of HSPCs
Fraction of Myeloblasts
Fraction of Megakaryocytes
ns (p = 0.055)
ns (p = 0.071)
ns (p = 0.095)
NBM (>50 y.o)
CHIP/CCUS
MDS-Low-Grade (MDS-LB)
MDS-High-Grade (MDS-IB)
d
Fraction of Maturing Myeloid Cells
Fraction of Promyelocytes
Fraction of Proerythroblasts
Fraction of Erythroid Normoblasts
ns (p = 0.114)
ns (p = 0.094)
ns (p = 0.104)
Non-MDS (>50 y.o) (NBM + CHIP/CCUS)
MDS-Low-Grade (MDS-LB)
MDS-Low-Grade (MDS-LB-SF3B1)
MDS-High-Grade (MDS-IB)
MDS-High-Grade (MDS-IB-TP53)
e
Myeloblasts
Normoblasts/MMCs
DAPI CD34 CD117 p53 CD71 CD15
f
DAPI p53 CD117 CD71
g
Maturing myeloid cells
Erythroid Normoblasts
HSPC
Promyelocyte
Myeloblasts
Proerythroblast
p53+ Proportion
h
WCM67 (NBM)
WCM22 (MDS-IB-TP53)
DAPI CD34 CD117 CD38 CD71 CD61 CD15
i
Megakaryocyte Area/Nuclei
NBM
MDS-Low-Grade/CHIP/CCUS
MDS-High-Grade
Mean Nulcei
Area (μm²)
Normal Megakaryocytes:
Area: 309.6 ± 70.2 μm²
Mean Nuclei: 2.7 ± 0.8
MDS-Low-Grade/CHIP/CCUS Megakaryocytes:
Area: 230.8 ± 75.5 μm²
Mean Nuclei: 2.0 ± 0.6
MDS-High-Grade Megakaryocytes:
Area: 150.7 ± 49.2 μm²
Mean Nuclei: 1.6 ± 0.7

Figure 1. Single cell proportional and morphological changes in MDS. a, Bone marrow trephine biopsy data collection schematic. **b**, Variations in cell type proportions across entire treatment-naïve cohort. MDS patients are divided broadly into low blast (MDS-Low-Grade/MDS-LB) and high blast (MDS-High-Grade/MDS-IB) sample groups, with *SF3B1* (n=11) and *TP53* (n=7, of 9 total) mutations as the most frequent genotypes in MDS-LB and MDS-IB respectively. Non-MDS samples categorized as clonal hematopoiesis of indeterminate potential/clonal cytopenia of undetermined significance (CHIP/CCUS), normal bone marrow (NBM; <50yrs or ≥50yrs). 12 cell types defined using phenotypic and morphologic parameters. **c**, Comparison of HSPC, myeloblast, and megakaryocyte proportions across primary sample groups (Mann-Whitney U-test; *p≤0.05, **p≤0.01, ***p≤0.001). **d**, Comparison of maturing myeloid cell (MMC), promyelocyte, proerythroblast, and erythroid normoblast proportions across sample groups, with additional MDS-IB stratification by *TP53* mutation status (Mann-Whitney U-test; *p≤0.05, **p≤0.01, ***p≤0.001). **e,** Representative MxIF image of putative *TP53*-mutated myeloblasts and erythroid normoblasts based on high p53 expression. **f,** Representative MxIF image of putative *TP53*-mutated CD117+CD71+ proerythroblasts. **g,** Proportions of cells identified with high p53 protein expression across all MDS-*TP53* samples in tissue microarray. **h,** Representative MxIF images from NBM and MDS samples showing significant differences in megakaryocyte size/morphology. **i,** Quantification of mean megakaryocyte cell area and number of nuclei across progression from NBM to high grade MDS samples shown as scatter plot with standard deviation values drawn as ellipses between NBM, CHIP/CCUS and MDS-LB, and MDS-IB. All MxIF images shown captured with Phenochart (v1.1, Akoya Biosciences).

Quantification of various hematopoietic cell types by MxIF analysis, including myeloblasts, promyelocytes, erythroid normoblasts, maturing myeloid cells (MMCs), and putative B-cell precursors, correlated positively with orthogonal measurements using conventional methods (e.g. manual cell counting, multiparameter flow cytometry [MFC]-based immunophenotyping) (**Extended Data Figure 1c, Supplementary Data Table 2**).

MxIF analysis further revealed differences in proportions of several rare cell types between NBMs, and treatment-naïve samples from the pathologic subgroups CHIP/CCUS, MDS-LB, and MDS-IB [**Figure 1b]**. The proportions of HSPCs, myeloblasts, and megakaryocytes increased commensurate with disease severity (**Figure 1c, Extended Data Figure 2a**); HSPC compartment expansion in MDS patients has been previously demonstrated using MFC performed on aspirated marrow samples.[12] As anticipated, putative B-cell precursors were depleted in MDS vs. non-MDS samples (**Extended Data Figure 2b**). Notably, MDS cases harboring *TP53* mutations were characterized by the most significant depletions in promyelocytes and MMCs, but the most significant increases in proerythroblasts and maturing erythroid normoblasts, particularly when compared to other MDS-IB samples (**Figure 1d**). Of note, we found no significant differences in the proportions of endothelial cells between all sample groups (**Extended Data Figure 2b**).

p53 protein labeling has been well-described as a method for identifying mutant p53 protein-containing cells (putative *TP53*-mutated cells) in tissue sections.[13–15] By coupling this approach with MxIF, we identified enrichment of *TP53*-mutated cells within the myeloblast, proerythroblast, and erythroid normoblast compartments (**Figure 1e-g**, **Extended Data Figure 2c**).

On manual review of MxIF image data, we observed a conspicuous increase in small, frequently mononuclear megakaryocytes in MDS-IB cases (**Figure 1h**). Quantification of megakaryocyte cell areas and mean nuclei detected per cell confirmed this impression (**Figure 1i**). Megakaryocytes expressing CD34 could be found in all sample groups and were consistently smaller in size than CD34-negative megakaryocytes (**Extended Data Figure 2d**)**;** interestingly, MDS-IB-*TP53* samples contained the greatest proportions of CD34-positive megakaryocytes. Similarly to megakaryocytes, erythroid normoblast cell areas were significantly larger in both MDS groups compared to age-matched NBMs and CHIP/CCUS samples **(Extended Data Figure 2e).** Interestingly, the sizes of proerythroblasts and promyelocytes correlated inversely with IPSS-M scores, with the smallest of these cell types found in *TP53*-mutated samples **(Extended Data Figure 2f).**

HSPCs and early hematopoietic progenitors are progressively displaced from perivascular and para-trabecular zones along progression from clonal hematopoiesis to overt MDS

We previously demonstrated in NBMs that HSPCs are consistently localized proximal to bone trabeculae and

CD34+ endothelial cell-lined vasculature in both younger and older individuals.[11] However, HSPCs appeared displaced in MDS samples, prompting us to further interrogate this pattern using permutation testing (**Figure 2a-b**). HSPCs were found proximal (within 15µm) to vasculature in young and old NBMs, and in CHIP/CCUS samples, but significantly displaced in both MDS-LB and MDS-IB samples (**Figure 2c-e, Extended Data Figure 3a)**. Assessment of sample-level data revealed that roughly half of MDS-LB and MDS-IB samples had no evidence HSPC localization near vasculature; additionally, nearly all MDS-LB and MDS-IB samples showed no evidence of peri-vascular myeloblast localization (**Extended Data Figure 3a**). Permutation enrichment score analysis further indicated that HSPCs were *negatively* enriched with respect to vasculature at distances up to 40µm (**Extended Data Figure 4a**). We next investigated whether perivascular enrichment patterns differed between wild-type and clonal HSPCs, by again using p53 protein labeling to distinguish *TP53*-mutant from -WT HSPCs **(Figure 2f).** Remarkably, we found WT-HSPCs localized more closely with endothelial cells, whereas *TP53*-mutated HSPCs were severely displaced from endothelium (**Figure 2g-h, Extended Data Figure 3c**). This finding suggests that clonal HSPCs specifically drive the observed "global" pattern of HSPC displacement from perivascular regions, particularly in *TP53*-mutated samples.

Previous studies have shown the importance of secreted CXCL12 in inducing migration to the bone marrow niche of CXCR4-expressing HSPCs. CXCL12 can be expressed by endothelial cells and perivascular stromal cells,[16] however, while CXCL12 expression levels may be increased in MDS, HSPCs from MDS samples exhibit significantly reduced migration toward CXCL12 in vitro.[17,18] Based on re-analysis of several publicly available RNA sequencing and surface proteomic datasets,[17,19–21] we found consistently reduced CXCR4 gene and protein expression within HSPC compartments from MDS samples, relative to healthy controls **(Figure 2i-k, Extended Data Figure 5).** Notably, *CXCR4* was the only significantly downregulated gene within HSPC populations across all of the RNA sequencing datasets **(Figure 2j**).

Myeloblasts exhibited a perivascular exclusionary pattern similar to HSPCs, while other early granulocyte- (promyelocytes) and erythroid-committed (proerythroblasts) progenitors were only found to be significantly displaced in MDS-IB (**Figure 2c-e, Extended Data Figure 3a**). Conversely, putative B-cell precursors and megakaryocytes were consistently found proximal to vasculature in all sample groups, with megakaryocytes demonstrating a stronger enrichment pattern in MDS samples (**Figure 2c, Extended Data Figure 3a**). We have previously dissected mechanisms underlying perivascular niche localization and consequent maturation and function of megakaryocytes,[22] although it remains to be explored whether these pathways are fully maintained in the setting of MDS. Of note, erythroid normoblasts were negatively enriched with respect to endothelium in all groups (**Extended Data Figure 3a**). Collectively, these data indicate a remodeling of the immediate perivascular cell composition in MDS samples relative to NBMs (**Figure 2e**).

As we previously reported in NBMs, HSPCs, myeloblasts, and promyelocytes also exhibited consistent significant localization to para-trabecular regions in CHIP/CCUS samples **(Extended Data Figure 3b, 4b-c).** In contrast to their displacement from vasculature, HSPC localization to trabeculae was mostly conserved in MDS samples regardless of disease severity or genotype; average distance measurements and permutation score analysis revealed that the average distance from HSPCs to trabeculae segmentations increases in MDS-LB and MDS-IB samples, although in the majority of samples HSPCs remain more enriched than other hematopoietic cell types at a significant level. Conversely, assessment of these same statistics for myeloblasts and promyelocytes indicated a widespread disruption of normal localization of these cells to trabeculae in a large portion of MDS-LB and MDS-IB samples.

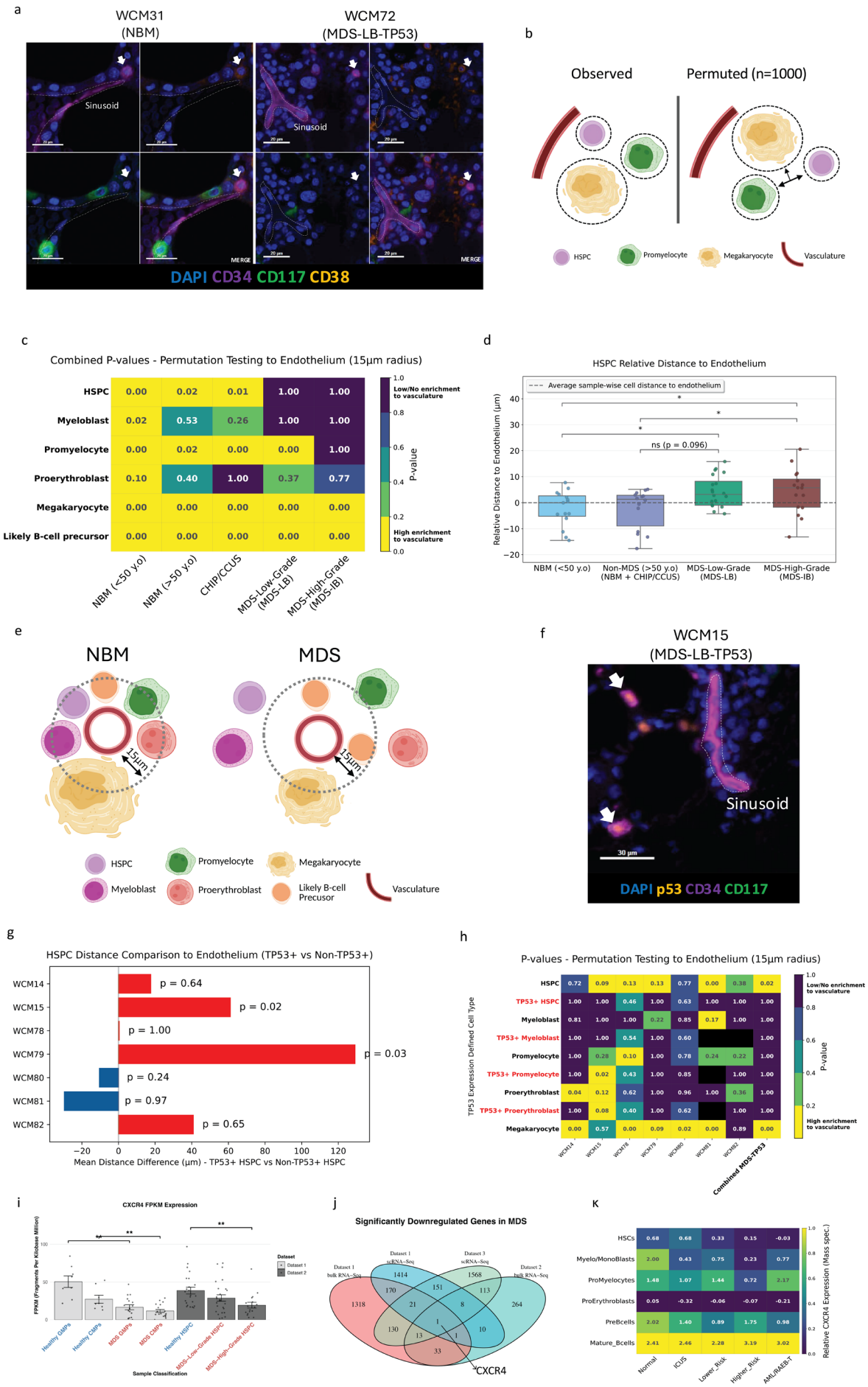
a
WCM31 (NBM)
WCM72 (MDS-LB-TP53)
Sinusoid
MERGE
DAPI CD34 CD117 CD38
b
Observed
Permuted (n=1000)
HSPC
Promyelocyte
Megakaryocyte
Vasculature
c
Combined P-values - Permutation Testing to Endothelium (15µm radius)
HSPC 0.00 0.02 0.01 1.00 1.00
Myeloblast 0.02 0.53 0.26 1.00 1.00
Promyelocyte 0.00 0.02 0.00 0.00 1.00
Proerythroblast 0.10 0.40 1.00 0.37 0.77
Megakaryocyte 0.00 0.00 0.00 0.00 0.00
Likely B-cell precursor 0.00 0.00 0.00 0.00 0.00
NBM (<50 y.o)
NBM (>50 y.o)
CHIP/CCUS
MDS-Low-Grade (MDS-LB)
MDS-High-Grade (MDS-IB)
Low/No enrichment to vasculature
High enrichment to vasculature
P-value
d
HSPC Relative Distance to Endothelium
Average sample-wise cell distance to endothelium
Relative Distance to Endothelium (µm)
ns (p = 0.096)
NBM (<50 y.o)
Non-MDS (>50 y.o) (NBM + CHIP/CCUS)
MDS-Low-Grade (MDS-LB)
MDS-High-Grade (MDS-IB)
e
NBM
MDS
15µm
HSPC
Promyelocyte
Megakaryocyte
Myeloblast
Proerythroblast
Likely B-cell Precusor
Vasculature
f
WCM15 (MDS-LB-TP53)
Sinusoid
30 µm
DAPI p53 CD34 CD117
g
HSPC Distance Comparison to Endothelium (TP53+ vs Non-TP53+)
WCM14 p = 0.64
WCM15 p = 0.02
WCM78 p = 1.00
WCM79 p = 0.03
WCM80 p = 0.24
WCM81 p = 0.97
WCM82 p = 0.65
Mean Distance Difference (µm) - TP53+ HSPC vs Non-TP53+ HSPC
h
P-values - Permutation Testing to Endothelium (15µm radius)
TP53 Expression Defined Cell Type
HSPC 0.72 0.09 0.13 0.13 0.77 0.00 0.38 0.02
TP53+ HSPC 1.00 1.00 0.46 1.00 0.63 1.00 1.00 1.00
Myeloblast 0.81 1.00 1.00 0.22 0.85 0.17 1.00 1.00
TP53+ Myeloblast 1.00 1.00 0.54 1.00 0.60 1.00
Promyelocyte 1.00 0.28 0.10 1.00 0.78 0.24 0.22 1.00
TP53+ Promyelocyte 1.00 0.02 0.43 1.00 0.85 1.00 1.00
Proerythroblast 0.04 0.12 0.62 1.00 0.96 1.00 0.36 1.00
TP53+ Proerythroblast 1.00 0.08 0.40 1.00 0.62 1.00 1.00
Megakaryocyte 0.00 0.57 0.00 0.09 0.02 0.00 0.89 0.00
WCM14 WCM15 WCM78 WCM79 WCM80 WCM81 WCM82 Combined MDS-TP53
Low/No enrichment to vasculature
High enrichment to vasculature
P-value
i
CXCR4 FPKM Expression
FPKM (Fragments Per Kilobase Million)
Healthy GMPs
Healthy CMPs
MDS GMPs
MDS CMPs
Healthy HSPC
MDS-Low-Grade HSPC
MDS-High-Grade HSPC
Sample Classification
Dataset
Dataset 1
Dataset 2
j
Significantly Downregulated Genes in MDS
Dataset 1 bulk RNA-Seq
Dataset 1 scRNA-Seq
Dataset 3 scRNA-Seq
Dataset 2 bulk RNA-Seq
CXCR4
k
HSCs 0.68 0.68 0.33 0.15 -0.03
Myelo/MonoBlasts 2.00 0.43 0.75 0.23 0.77
ProMyelocytes 1.48 1.07 1.44 0.72 2.17
ProErythroblasts 0.05 -0.32 -0.06 -0.07 -0.21
PreBcells 2.02 1.40 0.89 1.75 0.98
Mature_Bcells 2.41 2.46 2.28 3.19 3.02
Normal
ICLS
Lower_Risk
Higher_Risk
AML/RAEB-T
Relative CXCR4 Expression (Mass spec.)

Figure 2. HSPCs and early hematopoietic progenitors are progressively displaced from perivascular zones along progression from clonal hematopoiesis to overt MDS. a, Representative MxIF images of HSPC localization to (NBM) and displacement from (MDS) vasculature. **b,** Permutation testing spatial analysis metagraphical schematic **c,** Heatmap with p-values combined across sample groups (Stouffer's method) representing the significance of cell type localization to vasculature using 15um radius. Lower values (yellow) indicate significant spatial enrichment (cells closer to endothelium) as compared with randomly generated distribution, and higher values (blue) represent the lack of enrichment (cells further away/displaced from endothelium). **d,** Box plot and statistical test comparison (Mann-Whitney U-test; *p≤0.05, **p≤0.01, ***p≤0.001) of relative HSPC distance to endothelium as ratio of observed HSPC average distance to endothelium to average distance of all other hematopoietic cells within each sample. **e,** Cartoon schematic representing altered cellular composition in the perivascular niche as measured by permutation testing and other distance-based analysis observed in NBM versus MDS cases. **f,** Representative MxIF image of *TP53*-mutated MDS sample showing HSPCs with high p53 expression (putative *TP53*-mutated HSPCs) displaced from endothelium. **g,** Bar plot comparing the mean distance to endothelium of *TP53*-mutated versus –wild-type HSPCs detected across tissue microarray cohort samples. Red bars to the right indicate *TP53*-mutated HSPCs are more distant from vasculature in those samples. P-values shown for all samples. **h,** Permutation testing heatmap computed on tissue microarray cohort between cell type categories sub-defined by p53 expression. Low p-values (yellow) indicate association with endothelium as compared with high p-values (blue) indicating displacement from endothelium. **i,** *CXCR4* expression as measured by FPKM values computed from bulk RNA-Seq collected from publicly available data of CD34+ progenitors extracted from bone marrow biopsies of healthy and MDS patients (Adj. P =.008 in Healthy Granulocyte-Monocyte Progenitors [GMPs] vs MDS GMPs; Adj. P = .02 in Healthy Common Myeloid Progenitors [CMPs] vs MDS CMPs; Adj. P = .17 in Healthy HSPCs vs MDS-Low-Grade HSPCs; Adj. P = .008 in Healthy HSPCs vs MDS-High-Grade HSPCs). **j,** Combining differential expression tests across four datasets (two bulk RNA-Seq, two scRNAseq) yields *CXCR4* as only overlapping significantly down-regulated gene (FDR/p-val adj. < .05) across all datasets. **k,** Publicly available data quantification of CXCR4 protein expression by mass spectrometry. Mean sample group protein expression values plotted on heatmap with higher protein expression values in yellow. All MxIF images shown captured with Phenochart (v1.1, Akoya Biosciences).

Atypical erythroid island formation and early progenitor cell clustering in MDS

While erythroid normoblasts are normally found in well-formed maturation "islands" in NBMs, disaggregation of these structures is a recognized phenomenon and can be appreciated by light microscopy in MDS bone marrow tissues, particularly when the disease is advanced.[23–26] Indeed, on manual review of MxIF image data, we observed larger well-formed erythroid aggregates in NBMs, with conspicuous disaggregation in MDS-IB samples (**Figure 3a**). However, robust quantification of this phenomenon, especially at earlier stages of the disease, and correlation with clinical status and/or underlying genetics has not been previously described.

To analyze these patterns across all treatment-naïve samples and evaluate for differences between specimen classes, we employed Rolling Signal-based Ripley's K statistic, a metric used to quantify whether points in two-dimensional space tend to aggregate (high value) or be dispersed (low value), within defined radii (**Figure 3b**). Erythroid normoblasts were found to have the highest K-ratios in NBMs at all tested radii; conversely, the lowest K-ratios were observed in MDS-IB samples harboring *TP53* mutations (MDS-IB-*TP53*); the level of erythroid normoblast clustering in normal samples was roughly 50 percent greater than the K statistic in MDS-IB-*TP53* cases. However, MDS-LB samples harboring *SF3B1* mutations (MDS-LB-*SF3B1*) were also characterized by lower K-ratios than observed in *SF3B1*-WT/*TP53*-WT MDS-LB and MDS-IB samples (**Figure 3c**). Similarly, by erythroid cluster density analysis MDS-LB-*SF3B1* and MDS-IB-*TP53* samples were found to have the lowest density values (**Extended Data Figure 6**). These data suggest that erythroid island breakdown is a distinguishing feature of MDS topography compared to NBMs, but moreover, the degree of distortion may be related to genotype irrespective of histologic grade of disease. Interestingly, the K-ratio statistic correlated positively with peripheral blood hemoglobin values, suggesting a relationship between poor erythroid island formation and anemia (**Figure 3d**).

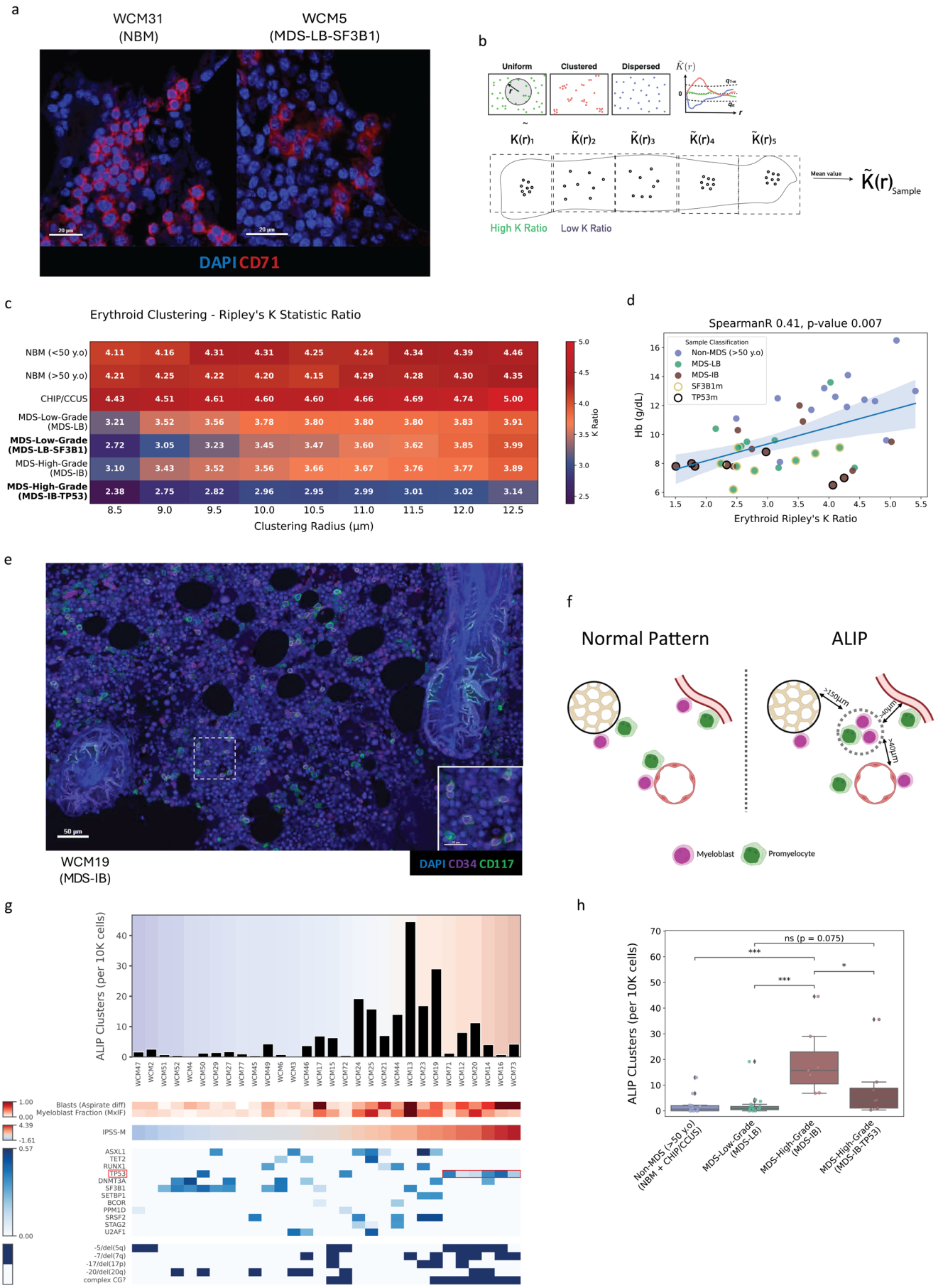
a
WCM31
(NBM)
WCM5
(MDS-LB-SF3B1)
20 µm
20 µm
DAPI CD71
b
Uniform
Clustered
Dispersed
$\tilde{K}(r)$
$q_{1-\alpha}$
q_{α}
0
r
$\tilde{K}(r)_1$
$\tilde{K}(r)_2$
$\tilde{K}(r)_3$
$\tilde{K}(r)_4$
$\tilde{K}(r)_5$
Mean value
$\tilde{K}(r)_{Sample}$
High K Ratio
Low K Ratio
c
Erythroid Clustering - Ripley's K Statistic Ratio
NBM (<50 y.o) 4.11 4.16 4.31 4.31 4.25 4.24 4.34 4.39 4.46
NBM (>50 y.o) 4.21 4.25 4.22 4.20 4.15 4.29 4.28 4.30 4.35
CHIP/CCUS 4.43 4.51 4.61 4.60 4.60 4.66 4.69 4.74 5.00
MDS-Low-Grade (MDS-LB) 3.21 3.52 3.56 3.78 3.80 3.80 3.80 3.83 3.91
MDS-Low-Grade (MDS-LB-SF3B1) 2.72 3.05 3.23 3.45 3.47 3.60 3.62 3.85 3.99
MDS-High-Grade (MDS-IB) 3.10 3.43 3.52 3.56 3.66 3.67 3.76 3.77 3.89
MDS-High-Grade (MDS-IB-TP53) 2.38 2.75 2.82 2.96 2.95 2.99 3.01 3.02 3.14
8.5 9.0 9.5 10.0 10.5 11.0 11.5 12.0 12.5
Clustering Radius (µm)
5.0 4.5 4.0 3.5 3.0 2.5
K Ratio
d
SpearmanR 0.41, p-value 0.007
Sample Classification
Non-MDS (>50 y.o)
MDS-LB
MDS-IB
SF3B1m
TP53m
Hb (g/dL)
Erythroid Ripley's K Ratio
e
50 µm
WCM19
(MDS-IB)
DAPI CD34 CD117
f
Normal Pattern
ALIP
>150µm
>40µm
>40µm
Myeloblast
Promyelocyte
g
ALIP Clusters (per 10K cells)
WCM47 WCM2 WCM51 WCM52 WCM4 WCM50 WCM29 WCM27 WCM77 WCM45 WCM49 WCM6 WCM43 WCM46 WCM17 WCM15 WCM72 WCM24 WCM25 WCM21 WCM44 WCM13 WCM23 WCM19 WCM71 WCM12 WCM20 WCM14 WCM16 WCM73
Blasts (Aspirate diff)
Myeloblast Fraction (MxIF)
IPSS-M
ASXL1
TET2
RUNX1
TP53
DNMT3A
SF3B1
SETBP1
BCOR
PPM1D
SRSF2
STAG2
U2AF1
-5/del(5q)
-7/del(7q)
-17/del(17p)
-20/del(20q)
complex CG?
h
ALIP CLusters (per 10K cells)
ns (p = 0.075)
***
***
*
Non-MDS (>50 y.o) (NBM + CHIP/CCUS)
MDS-Low-Grade (MDS-LB)
MDS-High-Grade (MDS-IB)
MDS-High-Grade (MDS-IB-TP53)

Figure 3. Atypical erythroid island formation and early progenitor cell clustering in MDS. a, Representative image example with well-formed strongly aggregated erythroid island formation in an NBM sample (left) and disaggregated and sparsely arranged erythroid clustering in MDS-LB-SF3B1 sample (right) **b,** Schematic for testing Rolling Signal-based Ripley's K statistic (RSRK) across a WSI **c,** Heatmap with mean RSRK erythroid clustering statistic between genotype sub-defined sample groups at multiple radii. MDS-LB-SF3B1 and MDS-IB-TP53 samples notably have lower clustering value than NBM and clonal hematopoiesis samples and lower clustering value than non *SF3B1*-mutated MDS-LB and non-*TP53*-mutated MDS-IB samples **d,** Regression line scatter plot shows Ripley K statistic clustering value has significant (Spearman R = .41; P = .007) positive trend with patient Hemoglobin CBC value across MDS and age-matched Non-MDS cohort. MDS-LB-SF3B1 and MDS-IB-TP53 samples are highlighted with yellow and black circles respectively, trending with the lowest Hemoglobin values along with lowest erythroid clustering K statistic. **e,** Image example from MDS-IB case showing clusters of abnormal located immature precursors (ALIP) in BM tissue region distant from trabecular bone and endothelium **f,** Graphical schematic for determining ALIP clusters from myeloblast and promyelocyte clustering in locations > 150um from trabeculae and > 40 um from vasculature. **g,** Bar plot with quantification of ALIP clusters at the sample level in MDS cases (normalized as frequency of ALIP clusters per 10,000 total nucleated cells in sample). Annotated in heatmaps below each bar for each sample are manual counting-based blast count from the aspirate smear, the sample level myeloblast proportion determined from MxIF quantification, IPSS-M risk score, variant allele frequency for select mutated genes, and chromosomal abnormalities. **h,** MDS-IB samples show the highest frequencies of ALIP clusters (Mann-Whitney U-test; *p≤0.05, **p≤0.01, ***p≤0.001). All MxIF images shown captured with Phenochart (v1.1, Akoya Biosciences).

Atypical localization of immature precursors (ALIP) correlates with disease severity and discriminates TP53-mutated and -WT subtypes of high-risk MDS

As shown in our recent work and confirmed in this study, the most immature granulocyte progenitors are normally localized near bone trabeculae and vasculature in NBMs, with more mature progenitors enriched in intermedullary areas of the bone marrow.

Atypical localization of immature precursors (ALIP) is a histologic pattern originally recognized in conventional hematoxylin and eosin-stained bone marrow tissue, and later confirmed by single marker immunohistochemical studies, as abnormal clustering of myeloblasts and/or promyelocytes at undefined distances from bone and vasculature.[27,28] Importantly, early studies correlated the presence of ALIP with poor cytogenetic risk factors and inferior survival characteristics.[29] However, more detailed assessments of ALIP have been lacking.

As expected, we identified foci of ALIP in a subset of MDS samples (**Figure 3e**, representative example). To quantify this finding, we defined ALIP by the presence of two or more myeloblasts and/or promyelocytes clustered within 12µm of each other at a distance >150µm from bone trabeculae and >40µm from endothelium (**Figure 3f**). Among treatment-naïve MDS samples, ALIP cluster density was lowest in MDS-LB samples and highest in a large proportion of MDS-IB samples (**Figure 3g, Extended Data Figure 7**); this finding was retained when we corrected for sample cellularity. However, among MDS-IB samples, ALIP cluster density was lower in those defined by *TP53* mutations and the highest IPSS-M scores (**Figure 3h**). This finding provides additional evidence of genetically imprinted spatial heterogeneity in the microarchitecture of MDS-IB cases that may appear homogeneous by IPSS-M-based risk assessment.

Integration of single cell quantitative features and microarchitectural patterns to generate spatially informed MDS severity scores

We next aggregated all single cell-level and spatial pattern data into a composite parameter, which we termed the "MDS severity score" (MDSSS), to analyze tissue samples at the whole-slide and patch level. Dimensionality reduction by t-distributed Stochastic Neighbor Embedding (t-SNE) demonstrated essentially distinct clustering of NBMs and treatment-naïve MDS samples (**Figure 4a, Extended Data Figure 8a**). Interestingly, MDS-LB and MDS-IB samples lacking *TP53* mutations clustered similarly but according to IPSS-M scores, while *TP53*-mutated MDS samples formed a completely distinct group. Feature extraction analyses revealed many single cell parameters, spatial patterns, and marrow structural characteristics as determinants of the observed t-SNE distributions **(Figure 4b).**

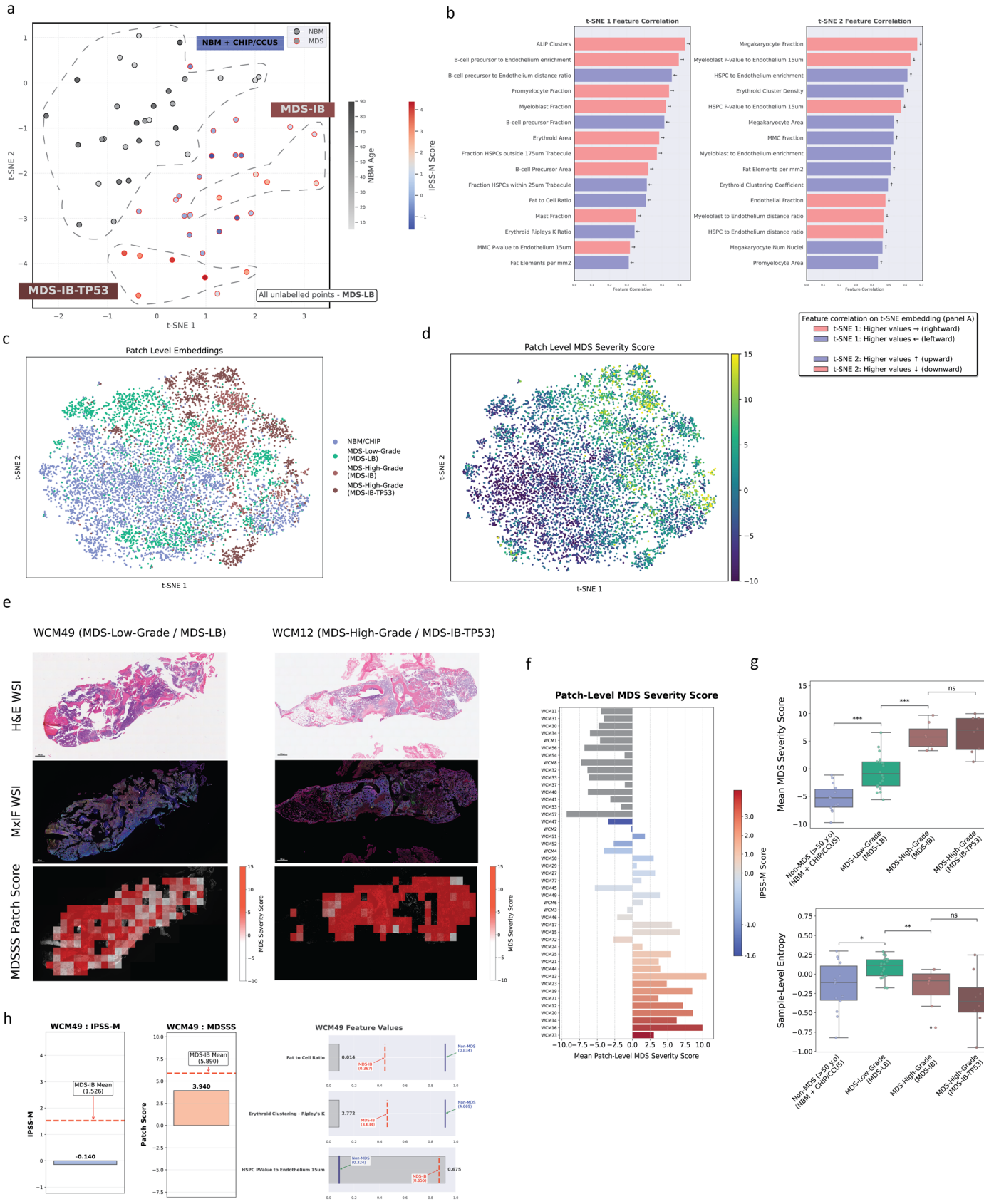
a
NBM + CHIP/CCUS
NBM
MDS
MDS-IB
MDS-IB-TP53
All unlabelled points - MDS-LB
NBM Age
IPSS-M Score
t-SNE 1
t-SNE 2
b
t-SNE 1 Feature Correlation
t-SNE 2 Feature Correlation
ALIP Clusters
B-cell precursor to Endothelium enrichment
B-cell precursor to Endothelium distance ratio
Promyelocyte Fraction
Myeloblast Fraction
B-cell precursor Fraction
Erythroid Area
Fraction HSPCs outside 175um Trabecule
B-cell Precursor Area
Fraction HSPCs within 25um Trabecule
Fat to Cell Ratio
Mast Fraction
Erythroid Ripleys K Ratio
MMC P-value to Endothelium 15um
Fat Elements per mm2
Megakaryocyte Fraction
Myeloblast P-value to Endothelium 15um
HSPC to Endothelium enrichment
Erythroid Cluster Density
HSPC P-value to Endothelium 15um
Megakaryocyte Area
MMC Fraction
Myeloblast to Endothelium enrichment
Fat Elements per mm2
Erythroid Clustering Coefficient
Endothelial Fraction
Myeloblast to Endothelium distance ratio
HSPC to Endothelium distance ratio
Megakaryocyte Num Nuclei
Promyelocyte Area
Feature Correlation
Feature correlation on t-SNE embedding (panel A)
t-SNE 1: Higher values → (rightward)
t-SNE 1: Higher values ← (leftward)
t-SNE 2: Higher values ↑ (upward)
t-SNE 2: Higher values ↓ (downward)
c
Patch Level Embeddings
NBM/CHIP
MDS-Low-Grade (MDS-LB)
MDS-High-Grade (MDS-IB)
MDS-High-Grade (MDS-IB-TP53)
t-SNE 1
t-SNE 2
d
Patch Level MDS Severity Score
t-SNE 1
t-SNE 2
e
WCM49 (MDS-Low-Grade / MDS-LB)
WCM12 (MDS-High-Grade / MDS-IB-TP53)
H&E WSI
MxIF WSI
MDSSS Patch Score
MDS Severity Score
f
Patch-Level MDS Severity Score
Mean Patch-Level MDS Severity Score
IPSS-M Score
g
Mean MDS Severity Score
Sample-Level Entropy
Non-MDS (>50 y.o) (NBM + CHIP/CCUS)
MDS-Low-Grade (MDS-LB)
MDS-High-Grade (MDS-IB)
MDS-High-Grade (MDS-IB-TP53)
ns
h
WCM49 : IPSS-M
MDS-IB Mean (1.526)
-0.140
IPSS-M
WCM49 : MDSSS
MDS-IB Mean (5.890)
3.940
Patch Score
WCM49 Feature Values
Fat to Cell Ratio
0.014
MDS-IB (0.367)
Non-MDS (0.834)
Erythroid Clustering - Ripley's K
2.772
MDS-IB (3.634)
Non-MDS (4.669)
HSPC PValue to Endothelium 15um
Non-MDS (0.324)
MDS-IB (0.655)
0.675

Figure 4. Integration of single cell quantitative features and microarchitectural patterns to generate spatially informed MDS severity scores (MDSSS). a, t-Distributed Stochastic Neighbor Embedding (t-SNE) dimensionality reduction plot of sample level data showing unique clustering pattern of MDS-IB and MDS-IB-TP53 samples in distant groups from NBM and clonal hematopoiesis samples. NBM samples are scaled in color by age, MDS samples are scaled in color by IPSS-M risk score. **b,** Bar plot showing top feature correlation with the t-SNE1 dimension (left) and top feature correlation with t-SNE2 dimension (right). Bars colored in red on t-SNE 1 plot represent features with highly positive correlation with t-SNE1 dimension, trending towards MDS-IB cluster generally. Bars colored in red on t-SNE 2 plot indicate highly positive correlation with t-SNE2 dimension, trending towards MDS-IB-TP53 generally. Bars colored in blue indicate highly negative correlation with t-SNE dimension. Arrows indicate direction of feature correlation on t-SNE plot x-y coordinates. **c,** t-SNE dimensionality reduction plot of 256x256µm patch-level data. Distribution of MDS sample derived patches are separated from NBM and clonal hematopoiesis sample derived patches in patterns indicative of disease severity. **d,** Patch-level MDS Severity Score (MDSSS), derived from 256x256µm patch-level data weighted by correlation with MDS disease severity in additive model, plotted as color coded feature plot on the patch-level t-SNE dimensionality reduction plot. **e,** Representative example of WSI of bone marrow core biopsy samples as H&E and MxIF images, and heatmap rendering across WSI sample region of patch-level MDSSS. Shown are two cases, WCM49 [MDS-LB] (left) and WCM12 [MDS-IB-*TP53*] (right). Higher patch scores colored in red. **f,** Bar plot with cases on the y-axis showing the mean patch-level MDSSS for all valid patches within each sample. Samples colored in grey are in NBM or clonal hematopoiesis sample groups. MDS samples are color coded by IPSS-M score according to the color bar on the right. 7 of 13 cases with IPSS-M <0 are MDSSS >0. **g,** Box plot and statistical comparison for mean MDSSS (top) and sample-level entropy of the MDS Severity Scores across patches of WSIs (bottom) [Mann-Whitney U-test; *$p \leq 0.05$, **$p \leq 0.01$, ***$p \leq 0.001$. **h,** Representative example of case WCM49 with low IPSS-M risk score and high MDS**SS**. Additionally, notable sample-level features shown, including fat to cell ratio, Ripley's K statistic clustering of erythroid normoblasts, and permutation testing derived p-value of HSPC localization to endothelium indicate a manifestation of more severe disease. All H&E and MxIF images shown captured with Phenochart (v1.1, Akoya Biosciences).

For example, NBMs were characterized by a higher proportion of putative B-cell precursors and their proximity to endothelium, HSPC enrichment near endothelium, larger/normally-nucleated megakaryocytes, higher fat to cell area ratios, and higher erythroid cluster densities. Conversely, key parameters for clustering of *TP53*-WT MDS samples included higher proportions of myeloblasts and promyelocytes, displacement of HSPCs from paratrabecular regions, and higher ALIP cluster densities. The distinct clustering of *TP53*-mutated MDS samples was notably driven by high proportions of megakaryocytes and significant displacement of HSPCs and myeloblasts from within 15µm of vasculature.

We next performed dimensionality reduction at the patch level (256µm square patches) using the same parameters across all cases (**Figure 4c, Extended Data Figure 8b**). This approach similarly revealed distinct clustering of *TP53*-mutated MDS patches from those extracted from NBM/CHIP/CCUS, and *TP53*-WT MDS samples. Similarly, *TP53*-WT MDS-IB patches clustered together, while patches from MDS-LB samples clustered heterogeneously, exhibiting some comingling with NBM/CHIP/CCUS patches (**Figure 4c**). Consistent with these distributions, the highest MDSSSs were associated with patches derived from all subtypes of MDS-IB (**Figure 4d**).

A heatmap analysis of patch-level MDSSS in individual treatment-naïve samples revealed intra-tissue heterogeneity (**Figure 4e**). Mean patch-level MDS severity scores generally increased commensurate with MDS grade, with the highest scores observed in *TP53*-mutated MDS samples **(Figure 4f-g).** MDS-LB samples were notably characterized by the highest sample-level entropy in patch-level severity scores (**Figure 4g**), indicating underappreciated spatial heterogeneity in microarchitectural perturbations found in MDS bone marrows, particularly at earlier stages of the disease. Indeed, we also identified focal high MDSSS patches in samples from CHIP/CCUS patients >50 years of age, likely representing a very early stage of disease elusive to detection using conventional diagnostic methods (**Extended Data Figure 8c**).

Interestingly, although IPSS-M and MDSSS values were aligned for most patients, we identified discordance in 7 of 13 patients, exemplified by IPSS-M scores <0 (lower risk) but MDSSS >0 (higher risk) [WCM6, WCM27, WCM29, WCM49, WCM50, WCM51, WCM77].

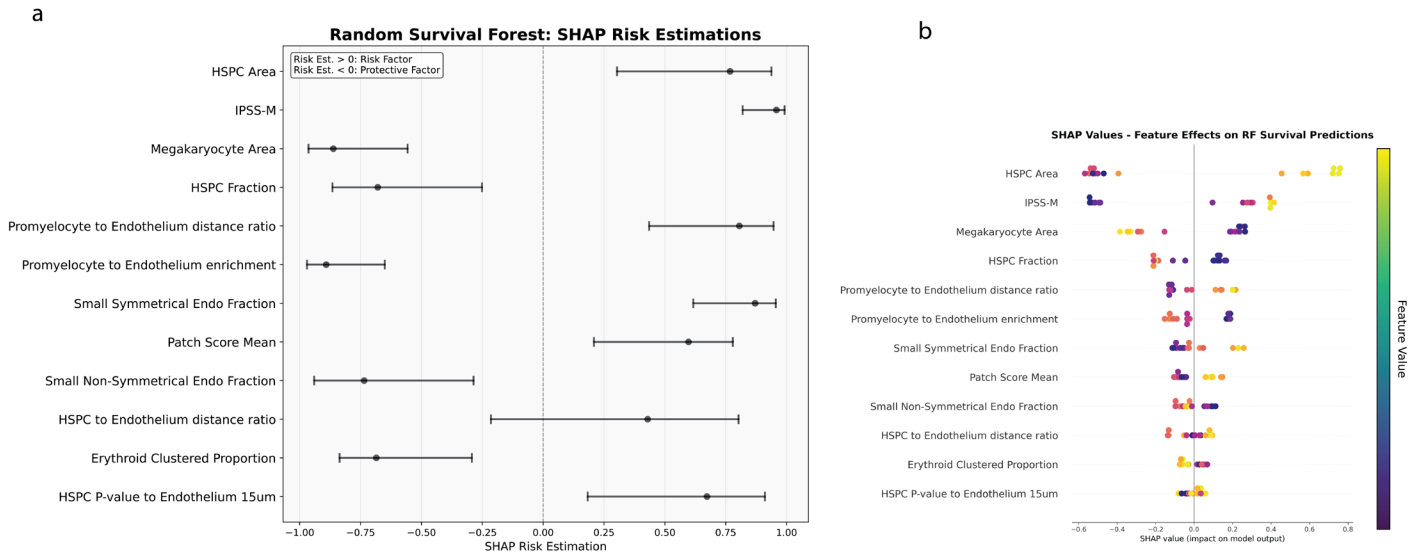

Figure 5. Correlation of cell morphologic and spatial features with blast progression. a, Forest plot with shapely value derived risk estimations of the 12 features used in random survival forest regression fit to patient outcome of blast count increase event post-treatment. For each feature, the dot location on the x-axis equates to the correlation between feature value and survival analysis model shapely value importance, as an estimation of risk, and the error bars equate to the confidence interval of the shapely value. Higher positive values correspond to higher risk estimation for a greater value of the feature, and lower negative values correspond to more protective estimation for a greater value of the feature. **b,** Shapely value bee swarm plot where dots are sample observations of each feature. Dot location on x-axis corresponds to the shapely value feature importance derived from our random survival forest modeling to patient blast count increase, and the color of the dot corresponds to the value of the feature per sample. Yellow colored dots farther to the right indicate higher feature values associated with higher shapely value importance for a positive observation of blast count increase, and yellow-colored dots farther to the left correspond to higher feature values associated with lower shapely value importance for negative observation of blast count increase.

Further examination of these cases revealed features commonly identified in higher risk samples (**Figure 4h**, representative example).

Correlation of cell morphologic and spatial features with blast progression

Although histomorphologic assessment of a bone marrow biopsy is required to establish a diagnosis of MDS, blast enumeration has remained the only parameter included in clinical prognostication models (e.g. IPSS-R, IPSS-M).[5,6] Therefore, we developed a machine learning pipeline to determine whether any of our extracted morphologic and spatial parameters could be associated with increased risk, or be considered protective, with respect to blast count increases in patients receiving DMTs (n=16) [**Supplementary Data Table 3**]**.** Higher IPSS-M values, larger HSPC size, promyelocyte and HSPC displacement from vasculature, and higher MDSSS values (patch score mean) were among features associated with disease progression; conversely, larger megakaryocytes, promyelocyte enrichment near vasculature, and higher erythroid normoblast clustering were found to be protective **(Figure 5, Extended Data Figure 9).** These findings indicate that histomorphologic features, particularly quantifiable spatial parameters unidentifiable by routine microscopic evaluation, may be relevant for predicting disease evolution and have additive value for risk assessment as currently performed using metrics such as the IPSS-M.

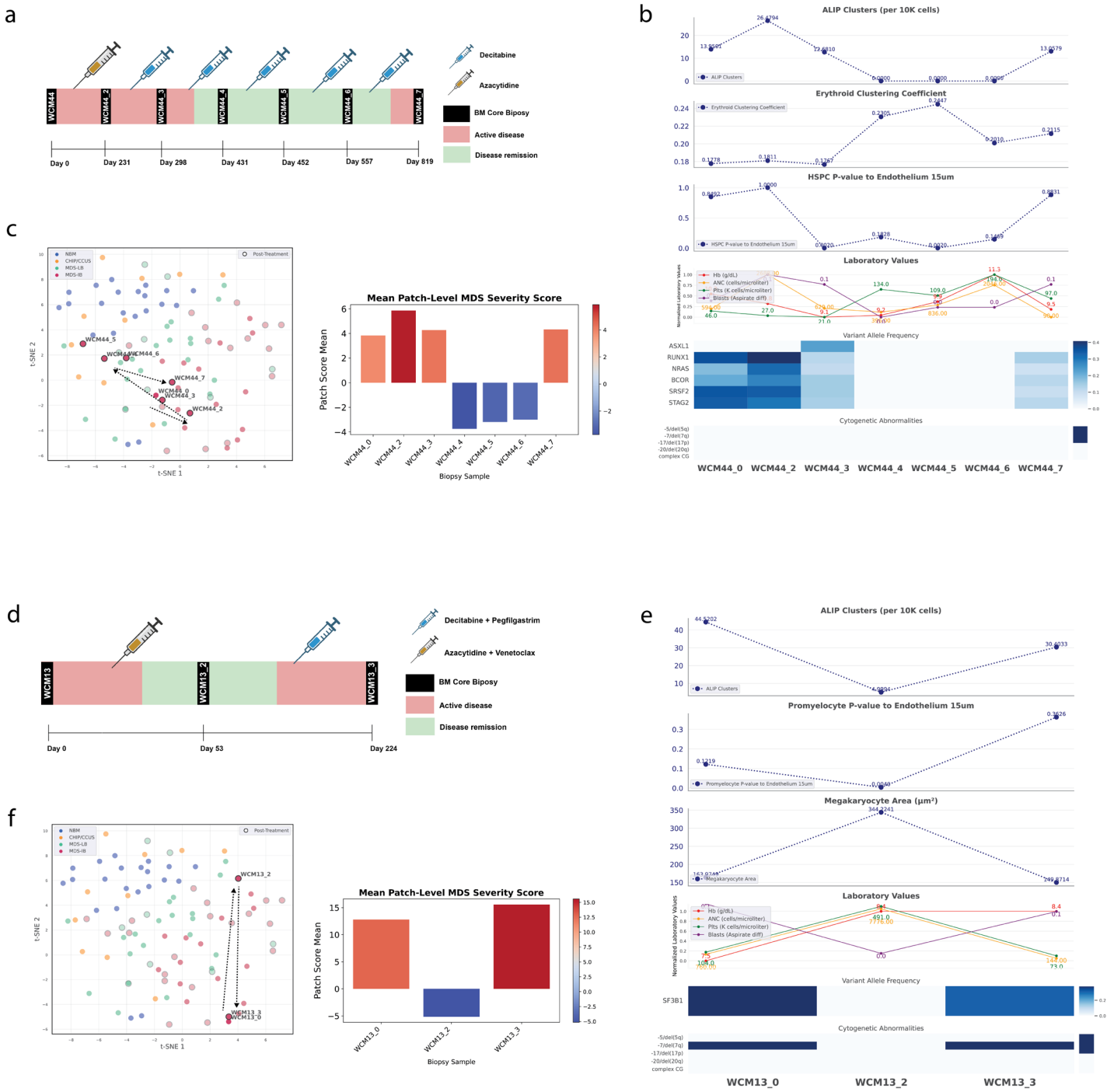

Figure 6. Multimodal longitudinal assessment in the course of disease modifying therapies. a, Timeline schematic illustrating course of clinical progression for patient WCM44. Red color bar value indicates active MDS disease presentation, and tan color bar value indicates disease remission. Black bars labelled sample identification represent bone marrow core biopsy performed at that time point. Administered treatments between time points are annotated with syringe icons. **b,** Line plots showing individual bone marrow core biopsy MxIF-derived features, ALIP clusters, erythroid clustering quantification, HSPC p-value in permutation testing to endothelium trend along with remission and reintroduction of genetic mutations along with improving and declining CBC values. **c,** t-SNE plot (right) traces WCM44 case samples along trajectory of disease treatment against sample-level embeddings of all Non-MDS and MDS samples. Post-treatment samples are highlighted with black circle. MDSSS bar plot (right), computed from features at the 256x256μm patch level and then averaged across the sample quantifies the severity of MDS disease presentation at bone marrow core biopsy time points. **d,** Timeline schematic for patient WCM13 with three bone marrow core biopsy samples indicating disease remission at timepoint 2 sample, WCM13_2. **e,** Line plots showing

individual features trend along with CBC values, SF3B1 variant allele frequency, and cytogenetic alterations in patient WCM13. **f,** t-SNE dimensionality reduction plot and MDSSS bar plot correlates with genetic and cytogenetic disease presentation in WCM13.

Multimodal longitudinal assessment in the course of disease modifying therapies

Longitudinal samples were analyzed for a subset of patients (n=14) who were treated with some combination of growth factor therapy, and hypomethylating agents, with or without venetoclax; three patients received allogeneic hematopoietic stem cell transplantation. Among patients who only received pharmacologic agents, only three achieved clinical remission during their treatment course (WCM2, WCM13, WCM44). A comprehensive assessment of single cell morphologic and spatial parameters in longitudinal samples revealed an NBM-like profile, with abrogation of various MDS-associated features (e.g. ALIP, HSPC displacement from vasculature), in bone marrow samples obtained at the time of transient clinical and molecular-cytogenetic remission **(Figure 6, Extended Data Figure 10).** Notably, reversion to an NBM-like profile was also observed in all three post-transplant samples from patients who received HSCT (WCM17, WCM21, WCM46).

WCM44 **(Figure 6a-c)** was characterized at diagnosis by a high mean patch-level MDSSS, high ALIP cluster density, low erythroid normoblast clustering coefficient, and HSPC displacement from perivascular regions. Following an initial period of persistent disease, pipeline analyses of samples collected during transient clinical and genetic remission revealed an absence of ALIP clusters, significant improvements in erythroid clustering coefficient values, HSPC enrichment near vascular endothelium, and negative patch-level mean MDS severity scores. However, these parameters returned to their baseline values at the time of disease recurrence, commensurate with clinical and genetic data. A similar pattern was observed for patient WCM13 (**Figure 6d-f)**, which was characterized by transient reversions of ALIP cluster density, megakaryocytic morphology, and promyelocyte localization to endothelium to NBM-like values at the time of clinical and genetic remission.

DISCUSSION

The microarchitecture of hematopoiesis in the bone marrow remains relatively poorly understood.[30] Although recent seminal studies using novel in situ imaging methods have begun to unravel the intricate spatial anatomy of murine hematopoiesis under steady-state and stress conditions,[31,32] achieving a similar understanding of the human system has historically posed significant challenges. Importantly, there are notable disease states for which reliable and widely-used models to study intact architecture do not exist,[9,10] and novel approaches are critically needed. Perhaps chief among these are myelodysplastic neoplasms (MDS).

Recently, we developed a method to study the microarchitecture of human hematopoiesis at single cell resolution using whole slide immunofluorescence-based imaging of human trephine biopsy tissues coupled with AI-based image analysis.[11] Our initial studies demonstrated a largely consistent spatial organization of key hematopoietic cell types along the aging spectrum, with relatively few architectural changes. Here, we aimed to address the nature and significance of perturbations in MDS in order to advance clinical assessment. Inclusion of serial bone marrow samples collected from patients treated using standard-of-care pharmacologic agents also permitted longitudinal tracking of microarchitectural changes, revealing key features with additional prognostic and disease monitoring potential.

We found that MDS is marked by an increase in hematopoietic stem and progenitor cells (HSPCs), early myeloid-committed progenitors (myeloblasts), and megakaryocytes, with this pattern intensifying as disease severity increases. Notably, MDS samples with *TP53* mutations show significant differences in proportions of erythroid and granulocytic progenitors, suggesting genotype-specific perturbations within hematopoietic lineages. Cytomorphological analysis revealed further insights: megakaryocytes, typically large and multi-nucleated in normal bone marrow,

become progressively smaller and mono-nucleated in MDS, correlating with diminishing platelet counts and other features of increasing disease severity. Of note, it has been widely reported that megakaryocytes are key components of the homeostatic bone marrow niche and function through paracrine modulation of HSPC proliferation or erythropoiesis.[33,34] Importantly, we observed the most significant megakaryocyte abnormalities in patients with *TP53*-mutated MDS, whose samples were also characterized by unique proportions of erythroid and granulocytic progenitors.

Our AI-based method was readily able to corroborate many of the typical changes in the hematopoietic compartment routinely identified using standard approaches (e.g. differential cell counting, flow cytometry) [**Figure 1a, Supplementary Figure 1c**]; however, these conventional approaches lack the capacity to dissect architectural changes, such as alterations in endothelial cell-lined vasculature and surrounding cellular composition. Importantly, our previous studies revealed that HSPCs are typically localized near trabecular bone and CD34-positive endothelial cells in normal marrow, supporting prior work that has shown non-dividing stem cells to be perisinusoidal.[35] Here, we found that HSPCs and myeloblasts are displaced from their usual perivascular location in MDS, while megakaryocytes and B-cell precursors remain largely unaffected.

The significance of endothelial cells in governing bone marrow hemostasis was initially described over twenty years ago,[36,37] and has been the subject of extensive research.[38,39] Our group has broadly contributed to the field, by demonstrating the modulatory role of endothelial cells through secretion of angiocrine factors that enable fine-tuned thrombopoiesis,[22] stem cell self-renewal,[40] regeneration of hematopoiesis following injury,[41] and balancing the fate of HSPCs.[42] The key architectural changes in the perivascular niche in MDS that we report in this study may be a driver of the clinical manifestations of the disease, particularly given that they correlate well with disease severity, and appear most pronounced in *TP53*-mutated patient samples.

In the quest for candidate molecular modulators of the observed HSPC displacement from endothelium, we focused on the CXCL12-CXCR4 axis, particularly because previous work has shown increased perivascular CXCL12 expression in MDS.[17,43,44] Interestingly, earlier studies demonstrated reduced migration of MDS HSPCs toward CXCL12 in vitro,[18] leading us to hypothesize that MDS HSPCs may have decreased CXCR4 expression. Indeed, using several publicly available datasets,[17,19–21] we found significantly and reproducibly lower CXCR4 gene and protein expression in MDS HSPCs compared to healthy controls. Additionally, given that p53 has been shown to participate in the modulation of CXCR4 levels,[45] it is not surprising that we found significant displacement of *TP53*-mutated HSPCs from endothelium as compared to their wild-type counterparts. Moreover, this finding points to a potential link between hematopoietic cell-intrinsic genetic defects and altered bone marrow architecture.

Historical studies have identified abnormal architectural features in MDS, such as disrupted erythroid islands and abnormal progenitor cell clustering,[23,27] but comprehensive characterization of these alterations has been lacking. Our analyses confirmed reduced erythroid cluster density in MDS, but surprisingly, lower cluster density was not exclusive to high-grade disease (e.g., *TP53*-mutated), as prominent erythroid island disruption was also a feature of low-grade *SF3B1*-mutated samples. Although the precise role of SF3B1 in establishing erythroid island architecture remains unknown, its role in erythropoiesis is well-recognized. Proper erythroid differentiation requires efficient SF3B1-dependent mRNA splicing,[46] while mutation-associated mis-splicing of key targets results in anemia.[47,48] Similarly, our observation of unique patterns of early progenitor cell clustering (ALIP) in MDS-IB patients with or without *TP53* mutations further suggest a link between genotype and microarchitecture.

To further quantify these microarchitectural changes, we combined single-cell and spatial data to generate an "MDS Severity Score" (MDSSS). In an analysis of treatment-naive samples, MDS samples clustered distinctly from normal bone marrow, with *TP53*-mutated samples showing unique clustering. MDSSS values aligned with IPSS-M scores in most cases; however, approximately half of IPSS-M lower risk patients were characterized by higher risk MDSSS values, indicating a potential for this metric to identify

patients whose disease course may not be accurately predicted using current models. Our analysis of patients who experienced disease progression further suggests that microarchitectural parameters, in addition to the clinical and hematologic parameters of the current models, could enable refined prognostication. Notably, patch-level MDSSS analyses revealed greater intra-tissue heterogeneity in low-grade MDS compared to high-grade or normal bone marrow samples, indicating that early MDS may exhibit more variable spatial changes, which could be overlooked in studies using aspirated marrow.

To test whether changes in bone marrow microarchitecture corresponded to clinical and genetic remission, we evaluated serial bone marrow samples collected from patients treated using standard-of-care pharmacologic agents. For patients who achieved remission, we observed architectural features reminiscent of an NBM-like state, including reduced ALIP density, re-localization of HSPCs near vasculature, and normalized megakaryocyte morphology. However, in patients with disease recurrence, these improvements reverted to baseline, reinforcing the connection between microarchitectural changes and disease state.

Here, we demonstrate the potential of high-resolution spatial biology to characterize hematopoiesis in MDS. Using an AI-driven approach to quantify microarchitectural alterations in patient samples, we identify genotype- and disease severity-specific patterns that are not captured by traditional histopathology. These findings have important implications for clinical practice and suggest that spatial analysis could be integrated into diagnostic workflows to enhance prognostication and treatment monitoring for MDS patients. Although further validation in clinical trials is needed, this approach holds promise for significantly improving the standard of care in MDS diagnosis and management.

REFERENCES

1. Cazzola, M. Myelodysplastic Syndromes. *N. Engl. J. Med.* **383**, 1358–1374 (2020).
2. Hasserjian, R. P., Germing, U. & Malcovati, L. Diagnosis and classification of myelodysplastic syndromes. *Blood* **142**, 2247–2257 (2023).
3. Yuen, L. D. & Hasserjian, R. P. Morphologic Characteristics of Myelodysplastic Syndromes. *Clin. Lab. Med.* **43**, 577–596 (2023).
4. Barone, P. & Patel, S. Myelodysplastic syndrome: Approach to diagnosis in the era of personalized medicine. *Semin. Diagn. Pathol.* **40**, 172–181 (2023).
5. Greenberg, P. L. *et al.* Revised International Prognostic Scoring System for Myelodysplastic Syndromes. *Blood* **120**, 2454–2465 (2012).
6. Bernard, E. *et al.* Molecular International Prognostic Scoring System for Myelodysplastic Syndromes. *NEJM Evid.* **1**, EVIDoa2200008 (2022).
7. Aster, J. C. What is in a Name? Consequences of the Classification Schism in Hematopathology. *J. Clin. Oncol.* (2023) doi:10.1200/JCO.22.02680.
8. Pronk, E. & Raaijmakers, M. H. G. P. The mesenchymal niche in MDS. *Blood* **133**, 1031–1038 (2019).
9. Mina, A., Pavletic, S. & Aplan, P. D. The evolution of preclinical models for myelodysplastic neoplasms. *Leukemia* **38**, 683–691 (2024).
10. Munteanu, R. *et al.* Humanized mouse models in MDS. *Cell Death Dis.* **16**, 531 (2025).
11. Sarachakov, A. *et al.* Spatial Mapping of Human Hematopoiesis at Single Cell Resolution Reveals Aging-

Associated Topographic Remodeling. *Blood* blood.2023021280 (2023) doi:10.1182/blood.2023021280.

12. Will, B. *et al.* Stem and progenitor cells in myelodysplastic syndromes show aberrant stage-specific expansion and harbor genetic and epigenetic alterations. *Blood* **120**, 2076–2086 (2012).
13. Fernandez-Pol, S., Ma, L., Ohgami, R. S. & Arber, D. A. Immunohistochemistry for p53 is a useful tool to identify cases of acute myeloid leukemia with myelodysplasia-related changes that are TP53 mutated, have complex karyotype, and have poor prognosis. *Mod. Pathol. Off. J. U. S. Can. Acad. Pathol. Inc* **30**, 382–392 (2017).
14. Tashakori, M. *et al.* TP53 copy number and protein expression inform mutation status across risk categories in acute myeloid leukemia. *Blood* **140**, 58–72 (2022).
15. McGraw, K. L. *et al.* Immunohistochemical pattern of p53 is a measure of TP53 mutation burden and adverse clinical outcome in myelodysplastic syndromes and secondary acute myeloid leukemia. *Haematologica* **101**, e320-323 (2016).
16. Möhle, R. *et al.* The Chemokine Receptor CXCR-4 Is Expressed on CD34+Hematopoietic Progenitors and Leukemic Cells and Mediates Transendothelial Migration Induced by Stromal Cell-Derived Factor-1. *Blood* **91**, 4523–4530 (1998).
17. Jann, J.-C. *et al.* Instructive interaction between myelodysplastic hematopoiesis and the bone marrow microenvironment at the single-cell level. *Blood Neoplasia* **1**, 100021 (2024).
18. Matsuda, M. *et al.* CD34+ progenitors from MDS patients are unresponsive to SDF-1, despite high levels of SDF-1 in bone marrow plasma. *Leukemia* **18**, 1038–1040 (2004).
19. Im, H. *et al.* Distinct transcriptomic and exomic abnormalities within myelodysplastic syndrome marrow cells. *Leuk. Lymphoma* **59**, 2952–2962 (2018).
20. Ganan-Gomez, I. *et al.* Stem cell architecture drives myelodysplastic syndrome progression and predicts response to venetoclax-based therapy. *Nat. Med.* **28**, 557–567 (2022).
21. Behbehani, G. K. *et al.* Profiling myelodysplastic syndromes by mass cytometry demonstrates abnormal progenitor cell phenotype and differentiation. *Cytometry B Clin. Cytom.* **98**, 131–145 (2020).
22. Avecilla, S. T. *et al.* Chemokine-mediated interaction of hematopoietic progenitors with the bone marrow vascular niche is required for thrombopoiesis. *Nat. Med.* **10**, 64–71 (2004).
23. Buesche, G. *et al.* Impaired formation of erythroblastic islands is associated with erythroid failure and poor prognosis in a significant proportion of patients with myelodysplastic syndromes. *Haematologica* **101**, e177–e181 (2016).
24. Kayano, H. Histopathology in the diagnosis of high-risk myelodysplastic syndromes. *J. Clin. Exp. Hematop. JCEH* **58**, 51–60 (2018).
25. Valent, P. *et al.* Normal and pathological erythropoiesis in adults: from gene regulation to targeted treatment concepts. *Haematologica* **103**, 1593–1603 (2018).
26. Zhang, J. *et al.* Identification of the haematopoietic stem cell niche and control of the niche size. *Nature* **425**, 836–841 (2003).

27. De Wolf-Peeters, C., Stessens, R., Desmet, V., Tricot, G. & Verwilghen, R. L. The histological characterization of ALIP in the myelodysplastic syndromes. *Pathol. Res. Pract.* **181**, 402–407 (1986).
28. Oriani, A. *et al.* Bone marrow histology and CD34 immunostaining in the prognostic evaluation of primary myelodysplastic syndromes. *Br. J. Haematol.* **92**, 360–364 (1996).
29. Della Porta, M. G. *et al.* Clinical Relevance of Bone Marrow Fibrosis and CD34-Positive Cell Clusters in Primary Myelodysplastic Syndromes. *J. Clin. Oncol.* **27**, 754–762 (2009).
30. Wu, Q., Zhang, J. & Lucas, D. Anatomy of Hematopoiesis and Local Microenvironments in the Bone Marrow. Where to? *Front. Immunol.* **12**, 768439 (2021).
31. Wu, Q. *et al.* Resilient anatomy and local plasticity of naive and stress haematopoiesis. *Nature* **627**, 839–846 (2024).
32. Zhang, J. *et al.* In situ mapping identifies distinct vascular niches for myelopoiesis. *Nature* **590**, 457–462 (2021).
33. Puhm, F., Laroche, A. & Boilard, E. Diversity of Megakaryocytes. *Arterioscler. Thromb. Vasc. Biol.* **43**, 2088–2098 (2023).
34. Di Giandomenico, S. *et al.* Megakaryocyte TGFβ1 partitions erythropoiesis into immature progenitor/stem cells and maturing precursors. *Blood* **136**, 1044–1054 (2020).
35. Acar, M. *et al.* Deep imaging of bone marrow shows non-dividing stem cells are mainly perisinusoidal. *Nature* **526**, 126–130 (2015).
36. Heissig, B. *et al.* Recruitment of stem and progenitor cells from the bone marrow niche requires MMP-9 mediated release of kit-ligand. *Cell* **109**, 625–637 (2002).
37. Rafii, S. *et al.* Human Bone Marrow Microvascular Endothelial Cells Support Long-Term Proliferation and Differentiation of Myeloid and Megakaryocytic Progenitors. *Blood* **86**, 3353–3363 (1995).
38. Gomez-Salinero, J. M., Redmond, D. & Rafii, S. Microenvironmental determinants of endothelial cell heterogeneity. *Nat. Rev. Mol. Cell Biol.* **26**, 476–495 (2025).
39. Pinho, S. & Frenette, P. S. Haematopoietic stem cell activity and interactions with the niche. *Nat. Rev. Mol. Cell Biol.* **20**, 303–320 (2019).
40. Butler, J. M. *et al.* Endothelial cells are essential for the self-renewal and repopulation of Notch-dependent hematopoietic stem cells. *Cell Stem Cell* **6**, 251–264 (2010).
41. Hooper, A. T. *et al.* Engraftment and reconstitution of hematopoiesis is dependent on VEGFR2-mediated regeneration of sinusoidal endothelial cells. *Cell Stem Cell* **4**, 263–274 (2009).
42. Kobayashi, H. *et al.* Angiocrine factors from Akt-activated endothelial cells balance self-renewal and differentiation of haematopoietic stem cells. *Nat. Cell Biol.* **12**, 1046–1056 (2010).
43. Flores-Figueroa, E., Varma, S., Montgomery, K., Greenberg, P. L. & Gratzinger, D. Distinctive contact between CD34+ hematopoietic progenitors and CXCL12+ CD271+ mesenchymal stromal cells in benign and myelodysplastic bone marrow. *Lab. Investig. J. Tech. Methods Pathol.* **92**, 1330–1341 (2012).

44. Abe-Suzuki, S. *et al.* CXCL12+ stromal cells as bone marrow niche for CD34+ hematopoietic cells and their association with disease progression in myelodysplastic syndromes. *Lab. Investig. J. Tech. Methods Pathol.* **94**, 1212–1223 (2014).
45. Li, Q. *et al.* Deletion of Wild-type p53 Facilitates Bone Metastatic Function by Blocking the AIP4 Mediated Ligand-Induced Degradation of CXCR4. *Front. Pharmacol.* **12**, 792293 (2021).
46. Moura, P. L. *et al.* Erythroid Differentiation Enhances RNA Mis-Splicing in SF3B1-Mutant Myelodysplastic Syndromes with Ring Sideroblasts. *Cancer Res.* **84**, 211–225 (2024).
47. De La Garza, A. *et al.* The splicing factor Sf3b1 regulates erythroid maturation and proliferation via TGFβ signaling in zebrafish. *Blood Adv.* **3**, 2093–2104 (2019).
48. Lieu, Y. K. *et al.* SF3B1 mutant-induced missplicing of MAP3K7 causes anemia in myelodysplastic syndromes. *Proc. Natl. Acad. Sci. U. S. A.* **119**, e2111703119 (2022).
49. Sarachakov, A. *et al.* Spatial mapping of human hematopoiesis at single-cell resolution reveals aging-associated topographic remodeling. *Blood* **142**, 2282–2295 (2023).

METHODS

Case Selection

Individuals who underwent a posterior iliac crest bone marrow biopsy, to evaluate for cytopenia of unknown etiology, were considered for inclusion in the study. Archival decalcified, bouin-fixed, and paraffin-embedded posterior iliac crest trephine bone marrow (BM) biopsy tissues were originally collected for routine diagnostic evaluation at Weill Cornell Medical College/NewYork-Presbyterian Hospital (WCM/NYP). Although two classification schema currently exist for MDS (World Health Organization 5th Edition [WHO] and International Consensus Classification [ICC]), WHO criteria were selected for streamlining and unifying case labeling. The cohort included patients diagnosed with MDS or CHIP/CCUS (n=48), and serial samples (n=29) were collected for several patients (n=14, range 2-7 samples/patient). Normal bone marrow (NBM) controls from a recently published cohort were also included.[49] All samples from CHIP/CCUS and MDS patients had undergone a comprehensive diagnostic hematopathology evaluation, involving conventional histomorphologic assessment, flow cytometry and immunohistochemistry-based immunophenotyping, cytogenetic analysis, and targeted next-generation sequencing. Complete blood count (CBC) with differential were also collected for these patients.

Following Institutional Review Board (IRB) approval, and in accordance with the Declaration of Helsinki, archival trephine biopsy samples were further evaluated using a pipeline for whole slide multiplex immunofluorescence tissue staining, whole slide imaging, and artificial intelligence (AI)-based image analysis (**Figure 1a, Extended Data Figure 1a**). Hematoxylin and eosin (H&E)-stained preparations from all NBM, CHIP/CCUS, and MDS samples were re-reviewed (SSP) to ensure the material was of adequate quantity and quality to be utilized for subsequent testing. Whole slide images (WSIs) of each H&E-stained preparation were captured using the Vectra Polaris Automated Quantitative Pathology Imaging System (Akoya Biosciences, Marlborough, MA). Bone marrow samples from 7 additional MDS patients with*TP53* DNA binding domain missense mutations, along with 5 additional NBMs, were included in a tissue microarray (see below) for select analyses.

All MDS patients were treated as per standard-of-care, including non-disease-modifying interventions (e.g., therapeutic red cell and/or platelet transfusion, erythropoiesis stimulating agents), disease-modifying pharmacologic agents (DMTs, n=25; e.g., hypomethylating agents (HMAs) with or without venetoclax), and allogeneic hematopoietic stem cell transplantation (HSCT, n=3) in a small subset of patients **(Supplementary Data Table 1).** Per 2023 MDS International Working Group (IWG) response criteria, among 25 patients who received DMTs during

their disease course, 9 achieved at least limited count recovery (CRL). Among 18 patients with longitudinal bone marrow evaluations at our institution, 9 experienced progressive increases in marrow blast percentages while receiving DMTs (**Supplementary Data Table 3**).

Clinicopathologic and Laboratory Data

The electronic medical record (EMR) for each patient included in the study was reviewed to obtain data concurrent with the evaluated biopsy specimen, including time of collection, patient body mass index (BMI), and CBC data including hemoglobin concentration (Hb), mean corpuscular value (MCV), absolute neutrophil count (ANC), and platelet count (Plt). All diagnostic hematopathology reports were re-reviewed (SSP, JTG) to confirm the original diagnosis (NBM, CHIP/CCUS, or MDS), and to extract data related to manual aspirate differential counting, including myeloid to erythroid (M:E) ratios, and percentages of blasts, promyelocytes, proerythroblasts, granulocytes, monocytes, erythroid normoblasts, and plasma cells. An International Prognostic Scoring System-Molecular was calculated for all treatment-naive MDS samples.[6] Details for all samples are provided in **Supplemental Data Table 1**.

Tissue Microarray Construction

Formalin-fixed paraffin-embedded human bone marrow clot section material was used to create a tissue microarray (TMA). One-millimeter cores were extracted from original tissue blocks and deposited in duplicate or triplicate into a recipient paraffin block using Tissue-Tek® Quick-Ray™ 1mm (Ref: 8016). The TMA included samples from patients with *TP53*-mutated MDS-LB or MDS-IB (WCM14, WCM15, WCM78, WCM79, WCM80, WCM81, WCM82), including two patients also included in the main trephine biopsy cohort (WCM14, WCM15). All *TP53* mutations were located in the DNA binding domain, leading to mutant p53 protein accumulation detectable by immunohistochemistry. Five normal bone marrow samples were included as controls (WCM83, WCM84, WCM85, WCM86, WCM87).

Multiparameter Flow Cytometry (MFC)

Multiparameter flow cytometry (10-color) was performed using the EuroFlow panel design.[50] MFC results were analyzed with BD FACSDiva software (BD Biosciences, San Jose, CA). Gating was performed using forward scatter parameters (FSC-A/FSC-H) to identify singlets, CD45/Viability Dye to identify viable cells, and CD45 by side scatter (SSC) gating to identify blast, lymphocyte, monocyte, and granulocyte subpopulations. Orthogonal flow cytometry data were available for all samples included in the study (n=99), with consistent assessment of percentages of lymphocytes, granulocytes, and monocytes. A minimum of 200,000 events were collected for all samples. All flow cytometry data were re-reviewed (SSP) and percentages for the following cell populations were determined based on available markers on a per-case basis: mature lymphocytes, granulocytes, monocytes, CD34+/CD117+ myeloblasts, CD117+/CD15+ promyelocytes, total CD15+ cells, total CD71+ cells, CD117+/CD71+ proerythroblasts, likely B-cell precursors (hematogones), plasma cells, and mast cells. Details for all samples are provided in **Supplementary Data Table 2**.

Cytogenetic and Fluorescence In-Situ Hybridization (FISH) Studies

Conventional cytogenetic analysis was performed on G-banded metaphase cells prepared from bone marrow aspirate or lymph node cultures using standard techniques. Twenty metaphases were analyzed and the results were reported using the International System for Human Cytogenetic Nomenclature. Fluorescence in situ hybridization (FISH) was performed where indicated and as feasible using multiplex probes LSI D5S23/D5S721 (5p15.2)/EGR1 (5q31) and CEP 7/D7S486 (7q31), and single probes CEP 8 (8p11.1-q11.1), LSI D20S108 (20q12) (Vysis/Abbott Molecular Inc., Des Plaines, IL), and LSI TP53 (17p13.1, SO) (Vysis/Abbott Molecular Inc., Des Plaines, IL) to rule out monosomy 5/deletion 5q31, monosomy 7/deletion 7q31, trisomy 8, deletion 20q12, and *TP53* deletion, respectively. Two hundred interphase nuclei were screened for each probe. Cytogenetic data for are included in **Supplementary Data Table 1**.

Next-Generation Sequencing

A custom 45 gene NGS panel [Thunderstorm system, RainDance Technologies, Billerica, MA, USA] interrogating single nucleotide variants (SNVs) and insertion/deletions (InDels) was used to profile the majority of the bone marrow samples (n=47). Sequencing was

performed using Illumina MiSeq (v3 chemistry) and samples were run in duplicate. The analytical sensitivity for this assay was approximately 2% for SNV and 1% for InDels. In addition, TruSight Oncology 500 (TSO500) assay, a 523-gene hybridization capture–based panel (Illumina Inc., San Diego, CA, USA) was used to profile SNVs and InDels in the remaining bone marrow samples based on availability of retained cell pellets (n=32). DNA was extracted from cell pellets, library was prepared according to manufacturer's specifications, and sequencing was performed on the Illumina NovaSeq6000. Bioinformatic analysis was performed using Local App version 2.2 (Illumina). The analytical sensitivity of TSO500 assay for SNVs and indels was approximately 3% variant allele frequency. Both sequencing assays were New York State approved for clinical use. Details for all samples are provided in **Supplementary Data Table 4**.

Multiplex Immunofluorescence Tissue Staining

Multiplex immunofluorescence (MxIF) staining was performed using the Opal system (Akoya Biosciences, Marlborough, MA) as previously described.[49,51,52] 4-micron-thick, Bouin-fixed, paraffin-embedded whole-tissue sections were prepared from decalcified human bone marrow core biopsy specimens. Subsequent steps were performed in a Bond RX automated tissue stainer (Leica Biosystems, Buffalo Grove, IL). Slides were first deparaffinized prior to EDTA-based antigen retrieval (Leica ER2 solution, 20 minutes). A cyclical staining protocol was then performed using horseradish peroxidase-mediated deposition of tyramide-Opal fluorophore constructs (Akoya Biosciences, Marlborough, MA) in each cycle; between each cycle, a combination of heat, citrate-based epitope retrieval solution (Leica ER1), and Bond Wash Solution (Leica) was used to remove primary/secondary antibody complex. Finally, 4', 6-diamidino-2-phenylindole (Spectral DAPI, Akoya Biosciences) was applied per provided protocols to label nuclei. Antibodies were selected from a menu of extensively validated and clinically tested clones in our CLIA laboratory (Weill Cornell Medicine/NewYork-Presbyterian Hospital, New York, NY). The following panel of primary antibody/fluorophore pairs was applied to all cases, in sequential order: 1) Opal 480/CD71 (1:80, 10F11, Leica concentrate), 2) Opal 520/CD61 (Ready-to-use, 2F2, Leica), 3) Opal 570/anti-CD117 (1:100, D3W6Y, Cell Signaling), 4) Opal 620/CD38 (1:50, 38C03(SPC32), Invitrogen), 5) Opal 690/anti-CD34 (1:100, QBEND/10, Invitrogen), 6) Opal 780/CD15 (1:50, MMA, BD Biosciences). A slightly revised panel with Opal 620/CD38 replaced with Opal 620/anti-p53 (DO-7) was used to analyze the tissue microarray. All slides were cover-slipped using ProLong™ Diamond Antifade Mountant (Invitrogen). Whole slide image (WSI) scans were subsequently obtained at 20X magnification using the Vectra Polaris/PhenoImager Automated Quantitative Pathology Imaging System (Akoya Biosciences). WSIs were tiled in Phenochart (v1.1, Akoya Biosciences); image tiles were subsequently spectrally unmixed in InForm (v2.4.8, Akoya Biosciences). Unmixed tiles were finally fused together in HALO (v3.3.2541.231, Indica Labs, Albuquerque, NM) to generate a single multi-layered TIFF image file for each sample, which was used in downstream analyses. Spectrally-unmixed WSIs were parsed using the computational pipeline described below. Representative images presented in figures were generated using Phenochart (v1.1, Akoya Biosciences).

Artificial Intelligence (AI)-based Digital Image Analysis

We leveraged state-of-the-art computer vision techniques and open-source software to extract individual cell locations, morphology, phenotypes, and spatial patterns from WSIs. The goal was to perform segmentation in which the boundaries of individual cells are defined and assigned coordinates, create phenotypes according to cell morphology and membrane marker expression, to automate masking and identification of bone marrow components (vasculature, bone trabeculae, and fat), and to detect communities of cells associated with masked components such as erythroid islands, and Atypical Localization of Immature Precursors (ALIP) clusters.

For defining individual cell boundaries and x-y coordinates (segmentation), Convolutional Neural Networks (CNNs) are optimally designed to extract features from raw imaging data, in this case the multiplexed immunofluorescence signal, and learn binary mask representations. Binary masks are used to define regions of interest where 0 is background or absent, and 1 is present. The DeepCell application Mesmer (DeepCell v0.12.10),[53] a recently published model designed for multiplexed immunofluorescence segmentation, had the most accurate performance for both whole-cell and nuclear segmentation. We fine-tuned Mesmer to accurately segment individual cells in bone marrow tissue and used Mesmer to extract whole-cell and nuclear segmentation masks for each WSI. Comprehensive details regarding model training and architecture are provided in **Supplementary Data Table 5**.

Phenotyping cell identities consisted of training and validating a CNN-based classification model based on the probability of observed positive marker expression on the cell membrane. We mapped CNN feature extractions of images of single cells along with the computed binary whole-cell segmentation mask to 1/0 binary outputs representing positive and negative marker expression. A separate marker classification model was trained for a similar task of identifying cells with high p53 protein expression based on expert hematopathologist annotations.

Masking and identifying components of the bone marrow was also accomplished from CNN segmentation. Bone trabeculae and fat segmentation were generated from patched WSIs of all image channels, and endothelium masks were generated from the CD34 channel alone. This pipeline transformed the raw imaging data into segmentation maps and an associated dataset of the location, cell identity, morphology, and relation to structural elements for around 5 million single cells across the cohort of patient bone marrow biopsies. A summary of architectures, prediction methods, data sets, and validation is provided in **Supplementary Data Table 5**.

Segmentation

The Mesmer model architecture consists of a feature pyramid network connected to a ResNet50 CNN, which extracts learned representations of raw image data at multiple scales and combines features with separate semantic head structures into the predicted output, simultaneous inner distance and pixel-wise transformations. We adapted Mesmer's TissueNet dataset, an extensive collection of segmentation mask annotated immunofluorescence images from nine different organs to pretrain our segmentation model and then fine-tuned our model on manually curated annotated 256x256 pixel patches of our WSI MxIF bone marrow core biopsy images. The TissueNet dataset, which is originally composed of two-channels, a nuclear and membrane channel, was augmented to four channels with the nuclear channel, two membrane channels, and an empty fourth channel intended for accurate segmentation of Megakaryocytes (CD61+). After pretraining on this augmented TissueNet dataset and annotations, we fine-tuned the model for accurate bone marrow segmentation with our annotated patches transformed as four channels with DAPI, CD71 as the most common membrane channel, a stack of other membrane markers, and CD61 for Megakaryocyte segmentation. For continuous segmentation throughout the WSI, 256x256 pixel patches were transformed to segmentation masks with overlapping boundaries, an open-source patch-stitching algorithm based on the python library Dask-image was used to merge together cells segmented on the boundaries of patched images (**Extended Data Figure 1a**). Segmentation masks were validated with manual pathologist-verified annotations. Statistical accuracy is recorded in **Supplementary Data Table 5**.

Phenotyping

The CNN architecture used for membrane classification was a ResNet18 backbone with a Global Average Pooling layer feeding into a single neuron, which outputs a probability from 0-1 for whether there was a positive membrane signal on each single cell image for each membrane marker (CD71, CD61, CD117, CD38, CD34, CD15). ResNet18 provided accuracy of larger CNN models with computational efficiency optimal for the task of labelling each cell and membrane prediction. This architecture was initialized with ImageNet model weights and was trained with a dataset of manually annotated membrane classification images. Our model was statistically and manually verified for accuracy (see **Supplementary Data Table 5**). Input to membrane marker CNN consisted of three-channel images of individual cells, centered around the cell of interest, consisting of the binary labelled cell segmentation mask (for distinguishing cell contour), DAPI signal (for presence and location of nuclei), and individual membrane signal of the individual membrane channel (for positivity classification). We used these membrane positive signal probabilities to annotate cell identities based on vectors of ground truth signature expression of 10 different cell types. Cosine similarity determined the closest match in cell identity between the CNN generated prediction vector and each ground truth vector and, in this way, automatically assigned cell phenotype classifications for each single cell segmented. After phenotyping, categorized cell types were found with expected distributions of membrane marker MFI (**Extended Data Figure 1b**). This method was described in recently published work.[49]

We trained a separate CNN model using the same general model architecture and training for classifying p53 expression in the nucleus of cells segmented and phenotyped as part of the tissue microarray analysis. In this case the ResNet18 backbone fed into a Global Average Pooling layer, which was subsequently connected to three output

neurons, as opposed to one. Additionally, we manually annotated nuclear protein expression positivity in this case as opposed to membrane marker positivity. This multi-class classification model classified p53 expression in single cells into three categories, low/no expression, moderate expression, and high expression, based on expert hematopathologist annotations. Cells classified as having high p53 expression were considered as TP53+ (i.e. putative *TP53*-mutated cells) for downstream analyses.

Structural Masks Segmentation

To quantify and analyze the spatial patterns of segmented, phenotypically classified cells, structural masks were computed as 1/0 binary masks consisting of positive pixels for regions determined by CNN segmentation to constitute the endothelium, bone trabeculae, and fat. CNN-based structural mask segmentation was computed for endothelium, bone trabeculae, fat segmentation masks as described previously.[49]

In computing individual cell distances to structural masks, the cell centroid was adjusted based on the cell size to account for significant differences in the size of cells such as Megakaryocytes and HSPCs. The resulting cell boundary distance to endothelium and trabeculae masks therefore was approximated by subtracting the cell radius from the distance from closest point of the structural mask to the cell centroid. Distance calculations were done using OpenCV python library functions findCountours and pointPolygonTest.

Megakaryocyte and Erythroid Normoblast Morphologic Analyses

Morphologic statistics were computed from each individual cell segmentation mask. Area was computed at the individual cell level as the two-dimensional space covered by the positive pixel mask and then normalized to represent the area in square microns. Eccentricity, which describes how circular or oval-shaped a two-dimensional circle or ellipse is, was quantified by the ratio of the major axis to the minor axis as determined by fitting an ellipse to the shape of the individual cell segmentation mask. These statistics (area and eccentricity), were calculated for every nuclear mask element segmented in the same way. Additionally, for Megakaryocytes the number of total nuclei was determined by counting individual elements of the nuclear segmentation mask that fell within the area of the cell segmentation mask. OpenCV python library was used for all morphologic computations.

Permutation Testing

Permutation testing was used to quantify spatial enrichment of cell types in relation to specific structural components (endothelium, and bone trabeculae). This involved quantifying the distribution of cell locations to structural components as compared between observed and randomly reassigned cell x-y coordinates. Permutations were shuffled 1,000 times for robustness. All hematopoietic cell locations were used as coordinates for randomly generated cell identities, and cell phenotypes were sampled without replacement. P-values were determined as the frequency of permutations where the randomly shuffled cell assignments showed equal or greater proximity to the structural component. Therefore, the permutation testing P-value represents the probability against the null hypothesis that the given cell type population tested was not at all spatially enriched within a predefined distance (e.g., 15µm or 30µm) from the structural component. Given the distribution of vascular elements within the cellular milieu of the bone marrow, we used a radius of 15µm to assess spatial proximity of hematopoietic cells to vascular elements. Conversely, to assess for hematopoietic cell enrichment near trabeculae we employed a radius of 30µm because trabeculae are larger structures that more dramatically define the tissue structure. Python libraries Scimap and Scipy.spatial were used for permutation testing and distance computation.

Erythroid Cluster Density and Rolling Signal-based Ripley's K Statistic Analyses

We applied two spatial pattern analysis techniques to quantify the degree of clustering of Erythroid Normoblast within a WSI. In both cases Erythroid Normoblast locations were modeled as point patterns of x-y coordinates. Ripley's K function is a standard method for determining clustering of a point pattern and involves quantifying the occurrences of points within proximity to each other in a pattern as compared with a random theoretical distribution of the same number of points. Since in a WSI, thousands of Erythroid Normoblast points are distributed across a heterogeneous space, we used a method designed for such cases. Rolling Signal-based Ripley's K computes the K statistic within distinct regions of the tissue and averages together values

computed across sliding windows to quantify the K statistic in the whole tissue.[54] This K statistic was tested at multiple distance radii to observe how Erythroid Normoblast clustering distributions changed at sequential distance intervals, and square regions of 256x256µm were used as the window size for the rolling signal local computation. We designed the second method since the generally observed behavior of Erythroid Normoblasts is to form island-like clusters across the bone marrow. We used Hierarchical DBSCAN clustering, a density based unsupervised clustering method, to identify distinct clusters of Erythroid Normoblast coordinates throughout the tissue. Spatial statistics were calculated on the individual cluster level, such as the density of the number of points within the area covered by the cluster boundary and the clustering coefficient as computed from the nearest neighbor distances of the cluster graph. Python libraries Scikit-Learn, NetworkX, and hdbscan were used.

Atypical Localization of Immature Precursors Analysis

To quantify the feature of atypical localization of immature precursors (ALIPs), generally defined as immature myeloid progenitors located in central intertrabecular regions, we constructed a nearest neighbor graph of all Myeloblasts and Promyelocytes and set a connection distance threshold of 12 microns to distinguish clusters of immature myeloid progenitors (myeloblasts/promyelocytes). Clusters that were located greater than 150 microns from bone trabeculae and 40 microns from endothelium were classified as ALIP clusters.

Treatment Response/Blast Progression Analyses

To assess the relative importance of our cell intrinsic and spatially computed features, we used machine learning and feature importance methods on a subset of patients in our cohort for which disease-modifying therapy (DMT) was given and clinical outcomes recorded. A random forest survival model was chosen because the ensemble-based approach and intrinsic feature selection are optimal for datasets with a small sample size. We used a logistic regression screening approach to select only features with the highest importance for input into the survival model along with IPSS-M risk score as covariates. Shapely value additive modeling, a method of feature importance estimation that is optimal for decision-tree based algorithms, was applied to estimate risk or predictive importance of each feature. Python libraries Scikit-Learn and shap were used for survival analysis and feature importance.

MDS Severity Score Analysis

Because we observed spatial heterogeneity in the manifestation of MDS features, we split each WSI into smaller "patches" (256x256µm) to compute features at the patch level and maintain information inherent to the spatial biology. To quantify in a single metric the presentation of characteristic MDS features, we created the MDS Severity Score (MDSSS), which combined locally computed cell intrinsic, morphological, and spatially determined features in an additive model. For comparing mean MDSSS between WSI samples, we filtered out any region with less than 100 cells or a proportion of Non-Hematopoietic Elements greater than 95 percent. Sample level entropy was computed using normalized continuous entropy of the two-dimensional patch level MDSSS heatmap and represents the disorder or randomness of each WSI sample's score values. Patch size of 256x 256µm was determined as the most viable patch size with the highest spatial resolution after computing basic statistics for different increments of patch sizes. Patch-level MDSSS is the sum of patch-level feature observations weighted by these feature importance scores, and represents an individual score for each patch in a tissue sample.

ADDITIONAL REFERENCES

50. van Dongen, J. J. M. *et al.* EuroFlow antibody panels for standardized n-dimensional flow cytometric immunophenotyping of normal, reactive and malignant leukocytes. *Leukemia* **26**, 1908–1975 (2012).
51. Berry, S. *et al.* Analysis of multispectral imaging with the AstroPath platform informs efficacy of PD-1 blockade. *Science* **372**, eaba2609 (2021).
52. Patel, S. S. *et al.* The microenvironmental niche in classic Hodgkin lymphoma is enriched for CTLA-4-positive T cells that are PD-1-negative. *Blood* **134**, 2059–2069 (2019).
53. Greenwald, N. F. *et al.* Whole-cell segmentation of tissue images with human-level performance using large-scale data

annotation and deep learning. *Nat. Biotechnol.* **40**, 555–565 (2022).

54. Healy, C. P., Adler, F. R. & Deans, T. L. Rolling Signal-based Ripley's K: A new algorithm to identify spatial patterns in histological specimens. 2020.05.21.109314 Preprint at https://doi.org/10.1101/2020.05.21.109314 (2020).

DATA AVAILABILITY

All data and code will be deposited online following formal manuscript review.

AUTHOR CONTRIBUTIONS

Conceptualization: S.P. *Methodology*: R.N., D.R., S.P. *Formal analysis*: R.N., D.R. *Investigation*: R.N., A.K., J.C., A.R., I.V., C.U., J.J., F.S., J.P., C.M., L.Z., D.S., G.R., P.D., J.K., J.F., M.G., N.L., A.C., M.O., P.S., J.G., G.I., S.R., D.R., S.P., *Visualization*: R.N. *Resources*: N.L., G.I., S.R., S.P. *Writing*: R.N., S.P. *Supervision*: D.R., S.P. *Funding acquisition*: S.R., S.P.

FUNDING

S.R. is supported by funding from the NIH (R35HL150809).

COMPETING INTERESTS

The authors declare no competing interests relevant to this study.

ACKNOWLEDGEMENTS

This work was supported by the Department of Pathology and Laboratory Medicine, Weill Cornell Medical College (start-up funding to S.S.P.). Tissue staining and imaging was performed in the Multiparametric In Situ Imaging (MISI) Laboratory of the Department of Pathology and Laboratory Medicine, Weill Cornell Medical College.

EXTENDED DATA

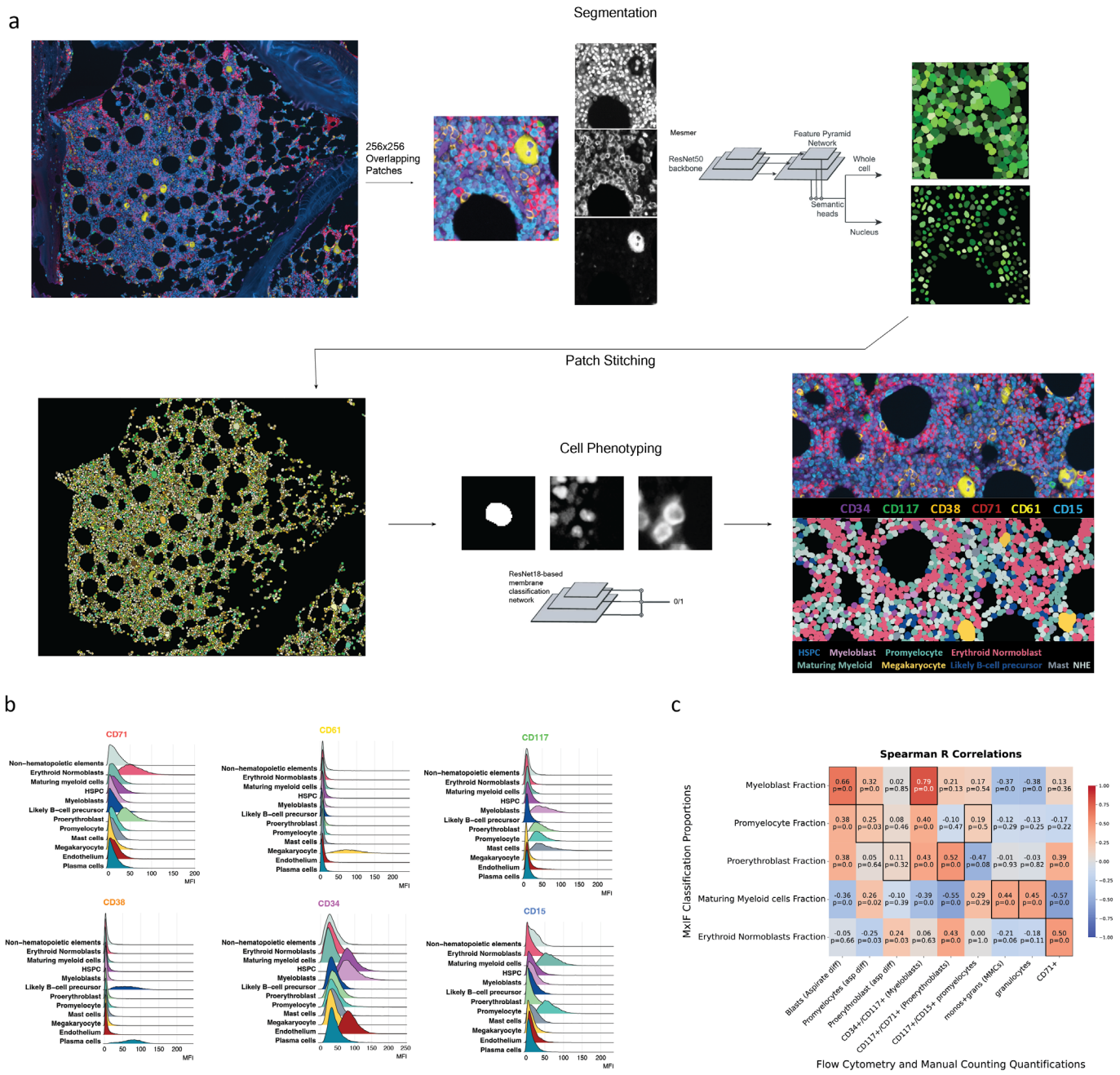

Extended Data Figure 1. a, Graphical schematic of AI-based digital analysis pipeline. Shown in image are original raw MxIF image, patch level segmentation, patch stitching for rendering full segmentation mask (bottom left). Cell phenotyping and associated segmentation-phenotype classification mask (bottom right) used for downstream analysis. **b,** Ridge plot of mean fluorescence intensity (MFI) quantification by cell type classification, calculated for validation of CNN-based binary labelling cell phenotyping algorithm. **c,** Correlation heatmap with Spearman R^2 and P-values comparing MxIF-derived cell proportion calculation to orthogonal manual cell counting- and flow cytometry-based quantifications.

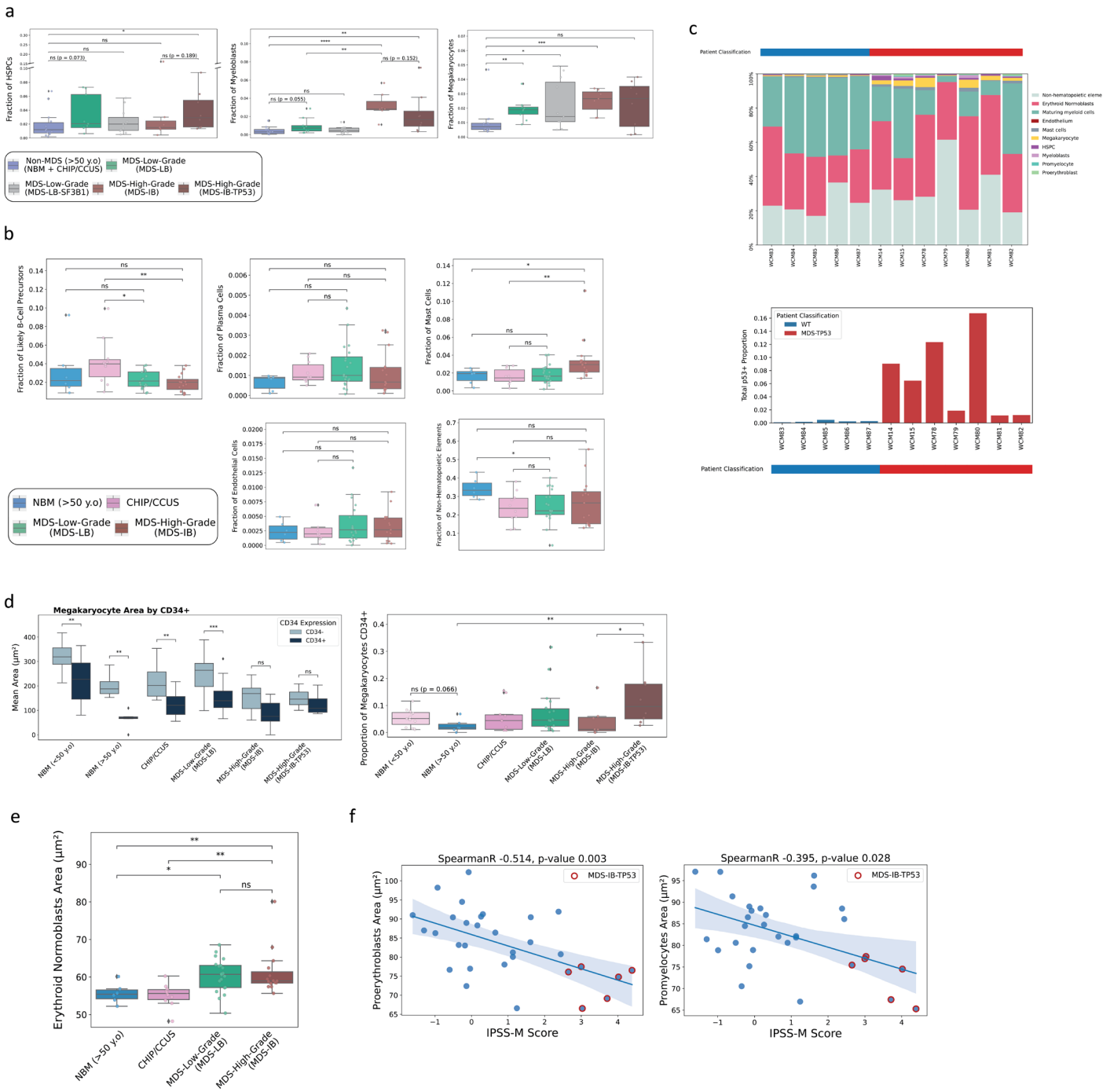

Extended Data Figure 2. a, Box plot and statistical test comparison (Mann-Whitney U-test; *p≤0.05, **p≤0.01, ***p≤0.001) for cell proportion quantification for HSPCs, myeloblasts, megakaryocytes between genotype sub-defined sample groups. **b,** Box plot and statistical comparison for cell proportion quantification for likely B-cell precursors, plasma cells, mast cells, endothelial cells, non-hematopoietic elements between sample groups. **c,** Stacked bar plot with cell proportion distributions for tissue microarray clot section samples and associated proportion of total cells with high p53 expression (putative *TP53*-mutated cells). **d,** Box plot comparing megakaryocyte cell area within sample groups split by CD34 expression. Associated comparison of proportion of CD34+ megakaryocytes (MFI > 60) by sample group. **e,** Box plot of erythroid normoblasts cell area between sample groups. **f,** Significant inverse correlation of proerythroblast and promyelocyte cell areas with IPSS-M risk scores. MDS-IB-*TP53* samples are annotated with red circles.

a

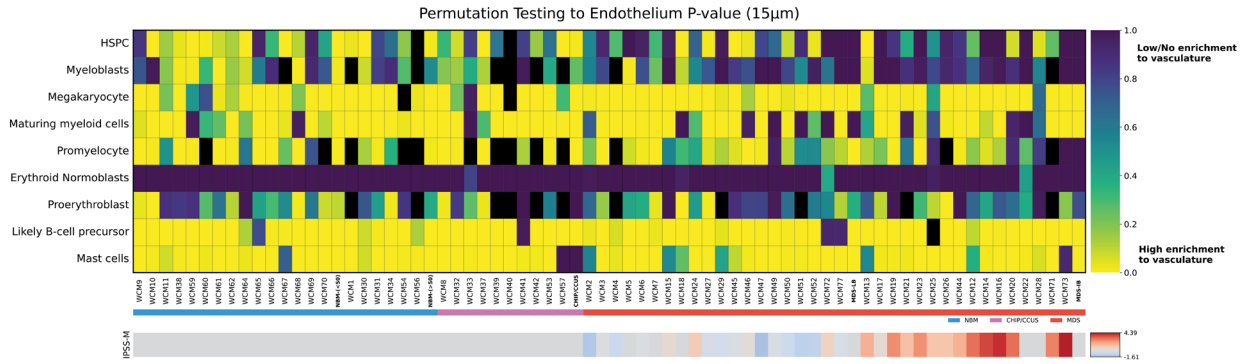

b

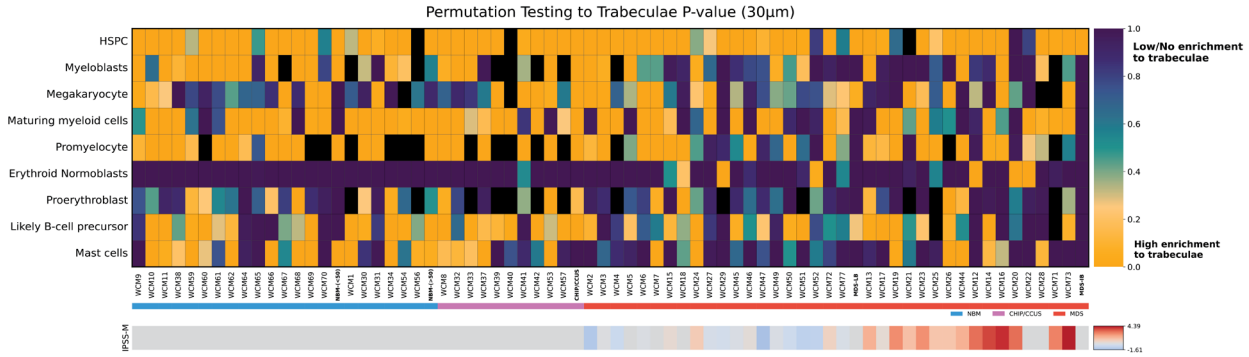

c

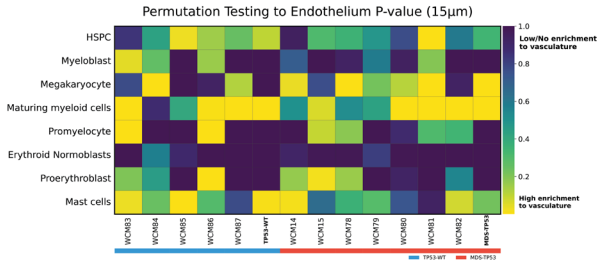

Extended Data Figure 3. a-b, Permutation testing p-value heatmaps showing enrichment of select cell types to endothelial mask (a) and trabecular mask (b) segmentations at the sample level. P-values are computed by comparing distance distribution between observed cell type locations within the specified mask radius and randomly shuffled distributions (n=1,000). A low P-value (yellow: endothlelium; orange: trabeculae) represents significant enrichment, and a high p-value (blue) indicates the lack of evidence of enrichment. Columns represent individual patient samples; rows contain P-values for denoted cells types. Columns in bold text along x-axis (NBM (< 50), NBM (≥50), CHIP/CCUS, MDS-LB, MDS-IB) are combined p-values within each sample group using Stouffer's method. **c** Permutation testing p-value heatmap computed using samples in clot section tissue microarray cohort containing *TP53*-mutated MDS and *TP53*-WT NBM samples. Columns represent individual patient samples; rows contain p-values for denoted cell types (yellow = low p-value). Columns in bold text along x-axis (*TP53*-WT, MDS-*TP53*) are combined p-values within each sample group.

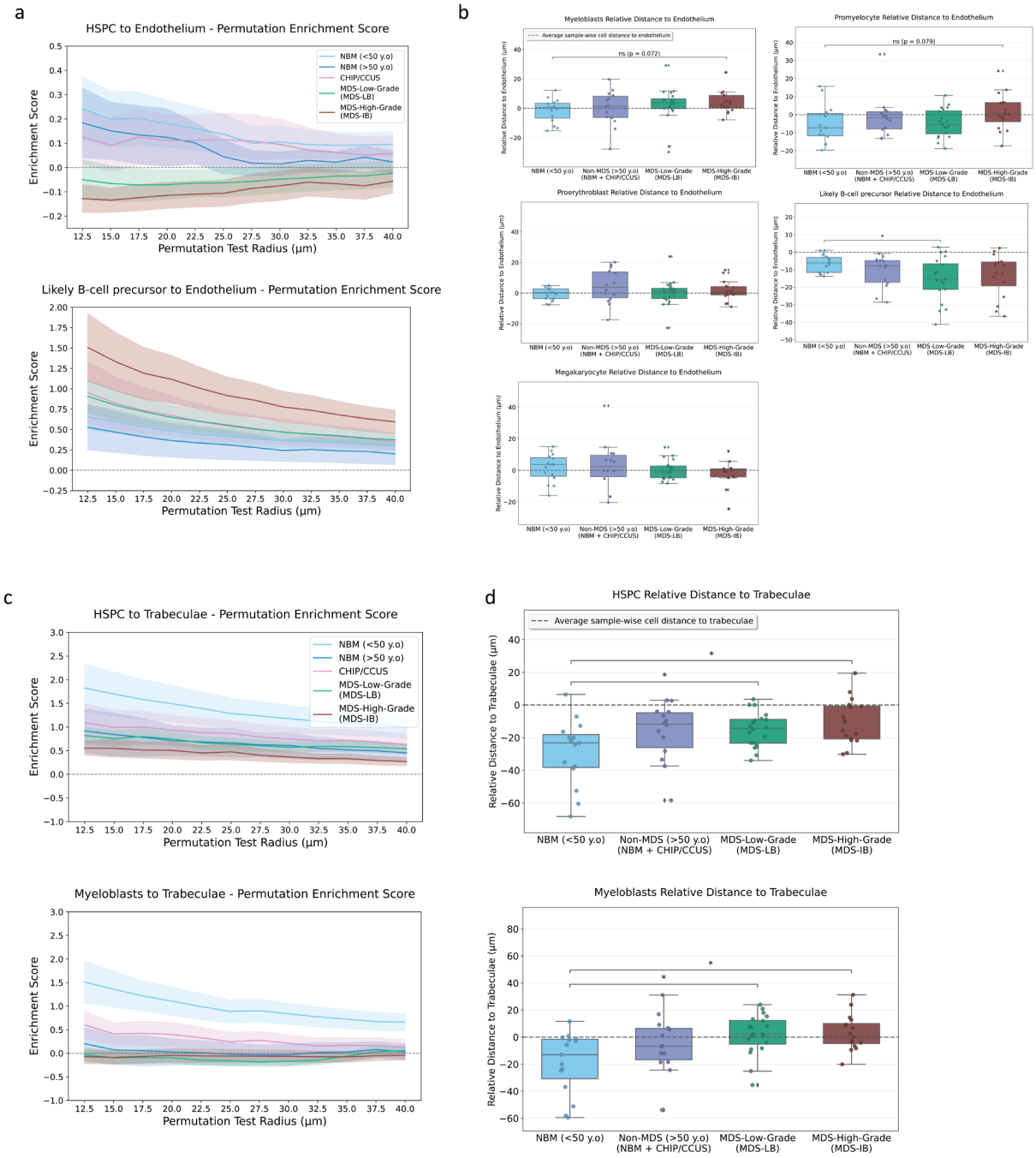

Extended Data Figure 4. a, Permutation enrichment line plot with ratio of observed HSPC (top), likely B-cell precursors (bottom) locations to endothelium to randomly shuffled locations at increasing radii. Dotted line drawn at enrichment score value 0 on y-axis represents an equal observed vs random distribution of localization to endothelium, positive values indicate enrichment to endothelium, and negative values represent lack of enrichment to/displacement from endothelium. **b,** Box plot and statistical test comparison (Mann-Whitney U-test; *p≤0.05, **p≤0.01, ***p≤0.001) of relative cell distance to endothelium as ratio of observed distance to endothelium for particular cell type to average distance of all other hematopoietic cells within each sample. Shown are myeloblasts, promyelocytes, proerythroblasts, likely b-cell precursors, and megakaryocyte distances. **c,** Permutation enrichment line plot with ratio of observed HSPC (top), myeloblasts (bottom) locations to trabeculae to randomly shuffled locations at increasing radii. **d,** Box plot and statistical test comparison of relative cell distance to trabeculae for HSPCs and myeloblasts.

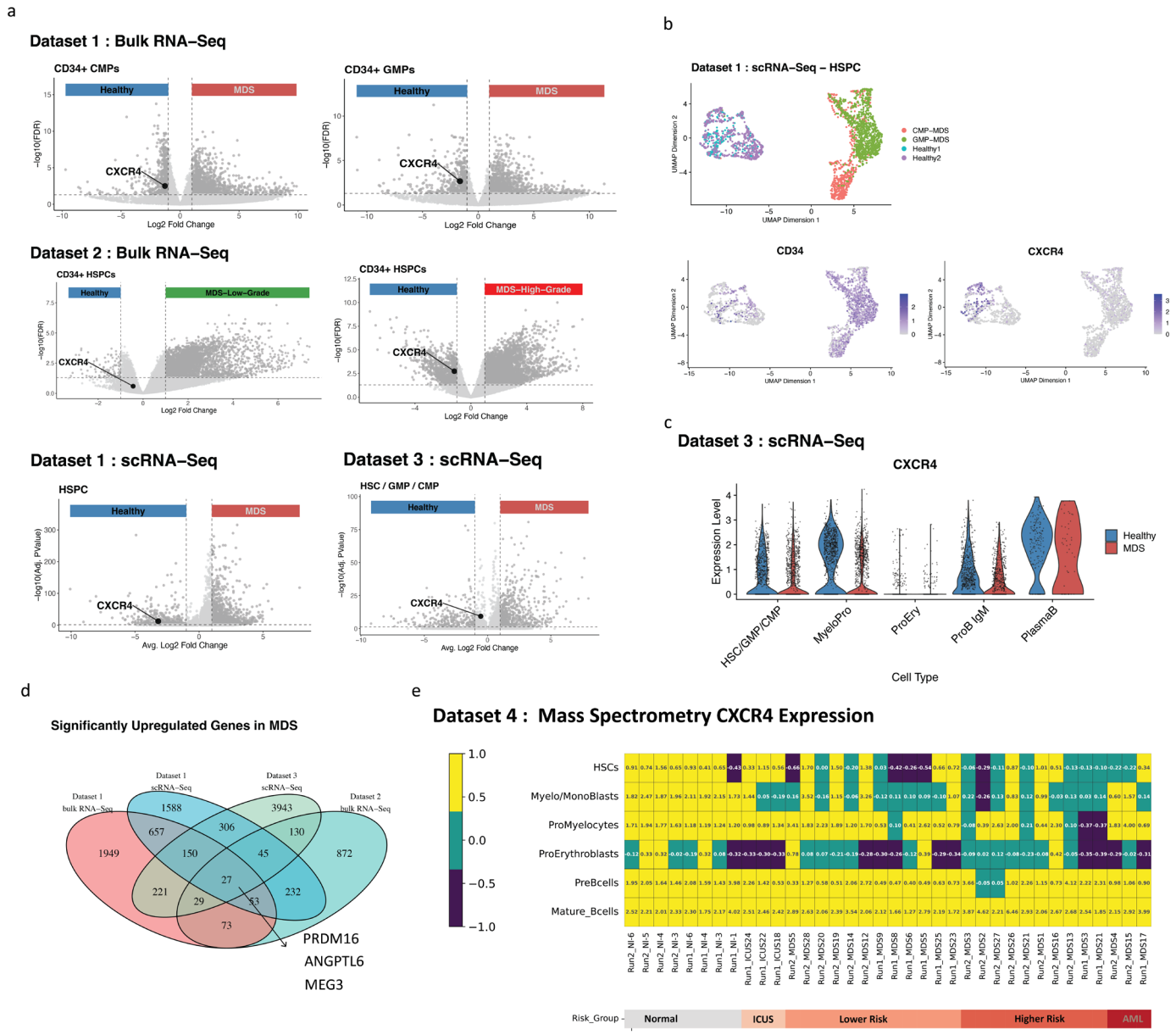

Extended Data Figure 5. a, Volcano plots for each dataset tested of CD34+ progenitor gene expression changes between NBM and MDS samples. CXCR4 is labelled with significant (FDR/Adj. P-value < .05) down-regulated in MDS in Dataset 1 CD34+ GMPs and CMPs, Dataset 2 MDS-High-Grade CD34+ HSPCs, Dataset 1 single-cell sequencing of CD34+ HSPCs, Dataset 3 single-cell sequencing of CD34+ HSPCs. Accession IDs for each gene expression dataset are as follows, Dataset 1: GSE136816, Dataset 2: GSE111085, Dataset 3: EGAS00001007568. **b,** UMAP plot with annotated sample labels among Dataset 1 single-cell sequencing of CD34+ HSPCs and associated feature plots of *CD34* and *CXCR4* gene expression. **c,** Dataset 3 single-cell sequencing derived violin plot of *CXCR4* gene expression split between Heathy and MDS conditions for labeled cell types. **d,** Venn diagram overlap of significantly differentially expressed genes from each RNA-Seq dataset based on testing of MDS vs Healthy CD34+ progenitors, with select genes labelled from total of 27 overlapped genes significantly overexpressed in MDS cases from each of these datasets. **e,** Sample level mass spectrometry quantification of CXCR4 protein expression on specific cell type populations as reported in Dataset 4. Columns represent samples recorded in Dataset 4 cohort and are annotated with color bar underneath sample indicating healthy (left-most samples) to high risk MDS/AML (right-most samples). Rows are cell types defined in this study. Higher values (yellow) indicate greater CXCR4 protein expression on the denoted cell type; lower values (grey and blue) indicate lower CXCR4 protein expression.

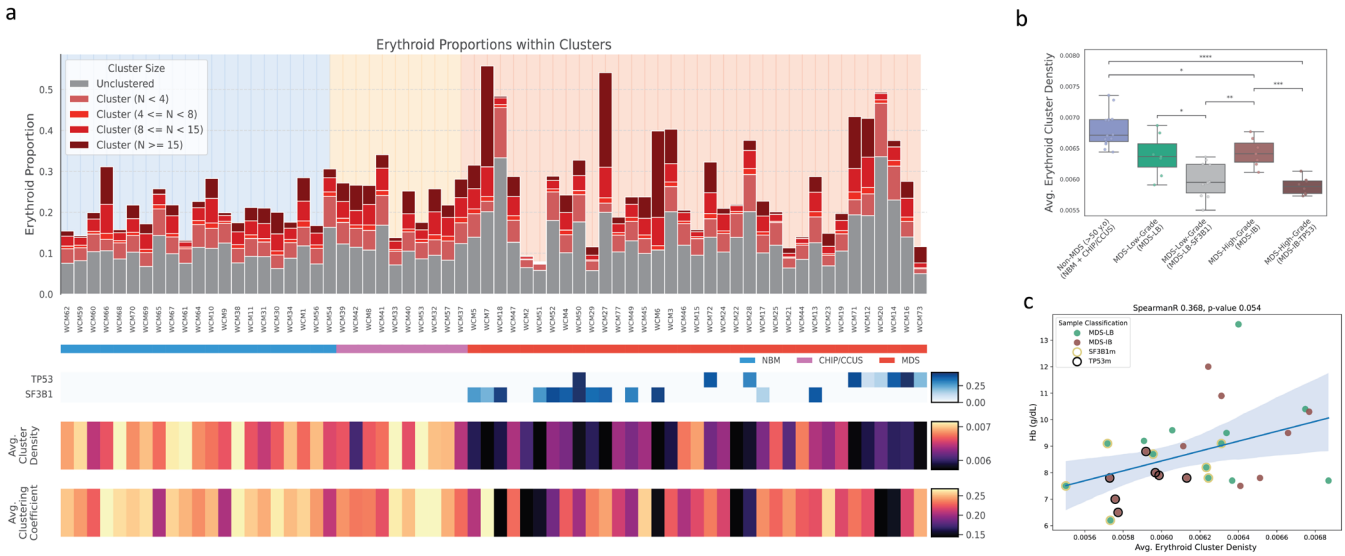

Extended Data Figure 6. a, Stacked bar plot displaying distribution of erythroid normoblast cluster sizes, obtained from HDBScan unsupervised clustering, represented as the proportion of total cells in each sample derived from erythroid normoblast clusters of each given size. Erythroid normoblasts that were not clustered or in a cluster of less than 4 cells are colored grey, and erythroid normoblasts clustered at increasing sizes are colored in red. Sample groups NBM (sorted by age), CHIP/CCUS, MDS (sorted by disease severity) are annotated in color bar below sample labels on x-axis. *TP53* and *SF3B1* mutation variant allele frequency is annotated for each sample. Average cluster density and clustering coefficient quantification calculated for each cluster is shown as a mean value among all (cluster size > 4) clusters within each patient sample listed on the x-axis. **b,** Box plot with statistical comparison of average cluster density between sample groups (Mann-Whitney U-test; *p≤0.05, **p≤0.01, ***p≤0.001). Lower average cluster density values indicate more dispersed erythroid normoblast clusters, while higher average cluster density values indicate more closely compact, well-formed erythroid normoblast clusters/islands. **c,** Average cluster density correlates positively with hemoglobin values within MDS-LB and MDS-IB sample groups. *TP53* and *SF3B1* mutated samples are annotated with black and yellow circles, respectively.

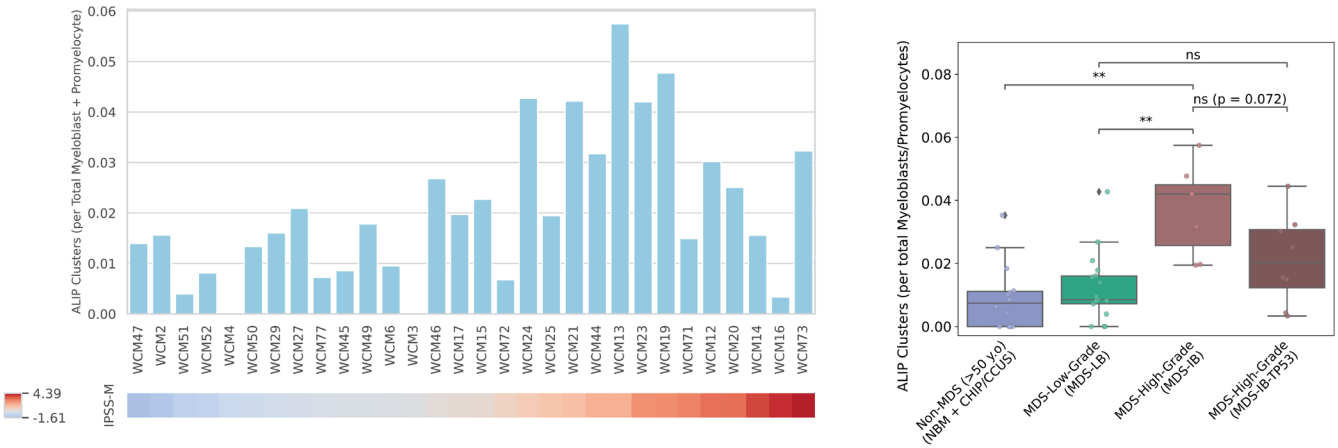

Extended Data Figure 7. Bar plot (left) with MDS samples on the x-axis and the ALIP cluster quantification normalized by total count of promyelocytes and myeloblasts on the y-axis. Box plot (right) and statistical comparison between genotype sub-defined groups of normalized ALIP clusters (Mann-Whitney U-test; *p≤0.05, **p≤0.01, ***p≤0.001).

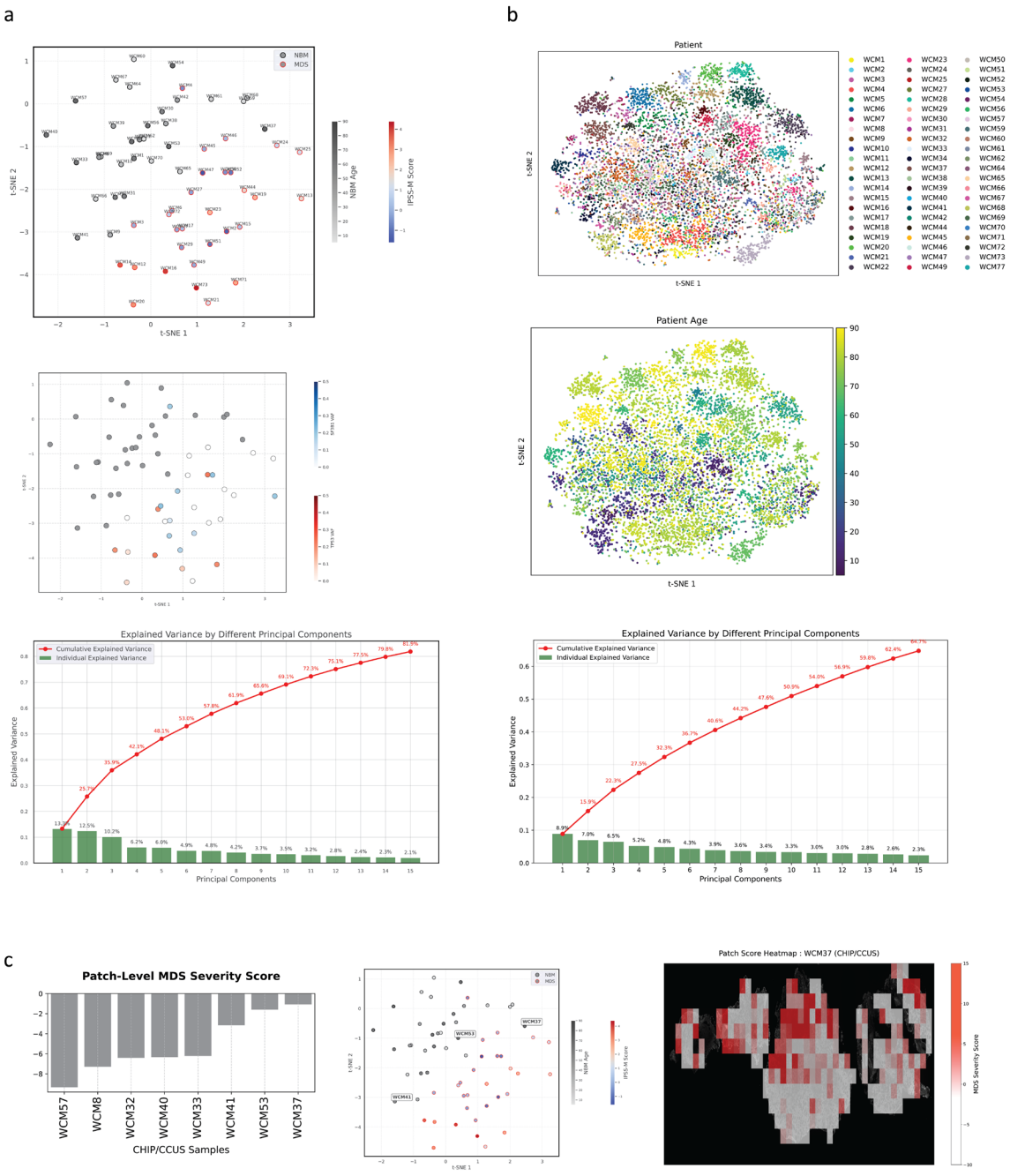

Extended Data Figure 8. a, t-SNE dimensionality reduction plot of sample-level features from panel 4A where each case is labelled. Below case labelled t-SNE plot is the same plot with TP53 and SF3B1 variant allele frequency values for each case, with distinct MDS-IB-TP53 cluster with lowest TSNE-2 values at the lower end of the plot axis. Additionally shown below is the total variance explained by principal component analysis for each component dimension for sample-level features. **b,** t-SNE dimensionality reduction plot using patch-level features from panel 4C where each case is labelled on each patch embedding. Shown below is the same plot with patient age on patch level features indicating a specific region of t-SNE plot with younger patient patches. Additionally shown below is the total variance explained by principal component analysis for each component dimension for patch-level features. **c,** Mean patch-level MDSSS compared among CHIP/CCUS samples, sorted in increasing MDSSS value order. Samples WCM41, WCM53, WCM37, chosen as relatively highest MDSSS among CHIP/CCUS cases, are plotted labelled on sample-level t-SNE plot along with NBM age, MDS IPSS-M color-coded sample embeddings. MDSSS patch-level score heatmap for WCM37 is shown where red squares indicate region of MDS-like features as evidenced by patch based additive model.

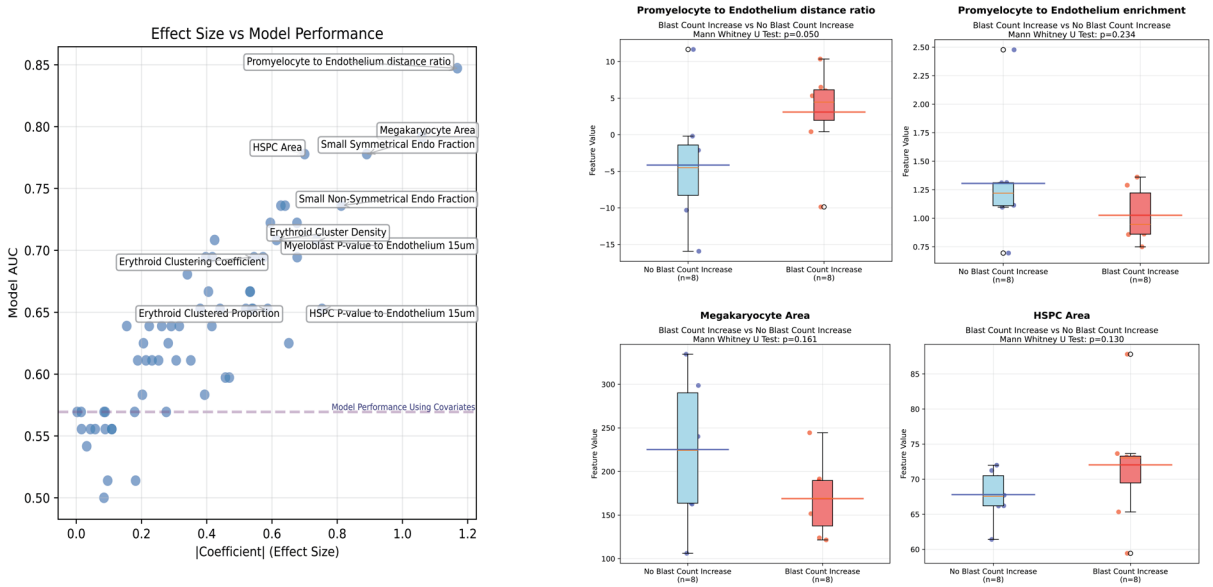

Extended Data Figure 9. On the left are features derived from logistic regression screening test that were further used for random forest survival analysis on patient blast count increase event outcome. X and Y axis are logistic regression model coefficient value and model AUC score respectively. Each dot is a feature and is plotted according to results from fitting individual logistic regression model of each feature and covariate to binary label of patient blast count increase event. Higher x-axis value indicates greater coefficient size (importance in fitting to blast count increase event) and higher y-axis value indicates greater model performance (accuracy in fitting to blast count increase event). The highest scoring features were used for subsequent random survival forest regression. On the right are four features, promyelocyte relative distance to endothelium, promyelocyte permutation enrichment to endothelium, megakaryocyte cell area, and hspc cell area, distinguished with higher feature importance in modeling patient blast count increase plotted as box plot with annotated statistical test results between patient group that did not experience blast count increase (n=8) and patient group that did experience blast count increase (n=8).

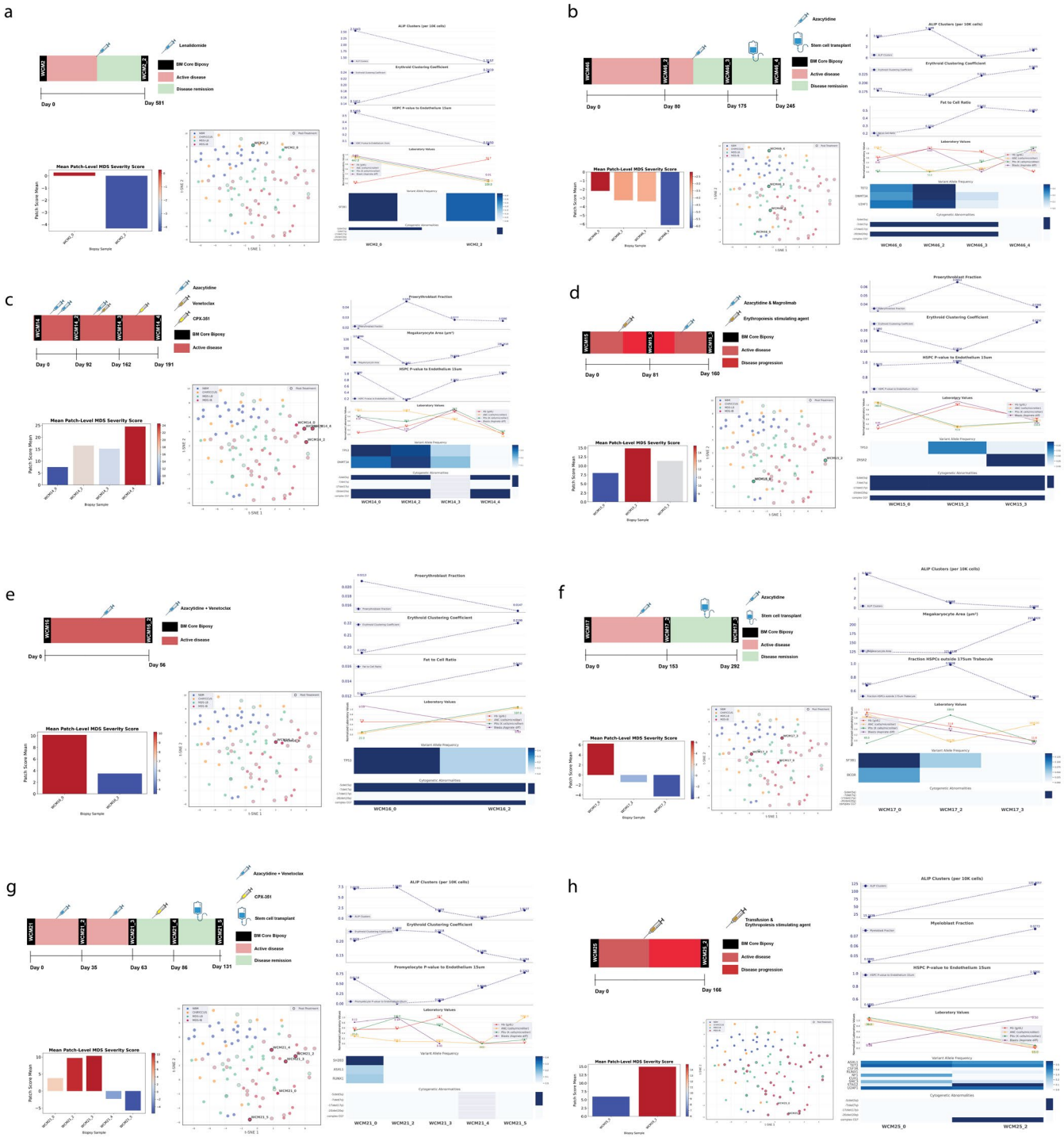

Extended Data Figure 10. a-h each represent a separate patient case. Longitudinal samples plotted as assessment of MDS associated MxIF imaging-based bone marrow microarchitectural perturbations. Timeline schematic illustrates general course of patient disease progression and administered treatment. t-SNE embedding shows dimensionality reduction where most healthy samples are located in the top left and further distance in x-y plane from healthy samples is indicative of overall more severe MDS pattern of features. Mean MDSSS, computed at the patch level, is plotted for each sample as quantitative assessment of MDS disease presentation in microarchitectural features. Individual features are plotted along with sample trajectory and compared against genetic and cytogenetic alterations and laboratory CBC values.